NASA Contractor Report 172481

Impact of Magnetic Isolation on Pointing System Performance in the Presence of Structural Flexibility

J. Sellers

Sperry Corporation
Phoenix, Az 85036

Contract NAS1-16909,
Task Number 2
February 1985

National Aeronautics and
Space Administration

Langley Research Center
Hampton, Virginia 23665

SPERRY CORPORATION
AEROSPACE & MARINE GROUP
P.O. BOX 21111
PHOENIX, ARIZONA 85036-1111
TELEPHONE (602) 869-2311

May 21, 1985

File: A0.1700

Subject: NASA Contractor Report 172481

Reference: NAS1-16909 Task Order No. 2

NATIONAL AERONAUTICS AND
SPACE ADMINISTRATION
Langley Research Center
Hampton, Virginia 23665

Attention: Mr. Richard Shisler
M/S 126

Dear Mr. Shisler:

Distribution has been completed in accordance with the enclosed distribution list for NASA Contractor Report #172481 entitled "Impact of Magnetic Isolation on Pointing System performance in the Presence of Structural Flexibility".

Sincerely,

R. E. Wallace
Contract Management Representative

REW/mc

enclosure

DISTRIBUTION LIST

NASA Contractor Report 172481

NAS1-16909-T2

Address	Number of Copies
NASA Langley Research Center Hampton, VA 23665	
Attn: 152/W. W. Anderson	1
161/A. Fontana	1
433/J. C. Gowdey	1
494/N. J. Groom	1
107/E. B. Pritchard	1
161/L. W. Taylor, Jr.	1
364/W. R. Hook	1
161/C. R. Keckler	20
151A/Research Information Office	2
NASA Goddard Space Flight Center Greenbelt, MD 20771	
Attn: 716.2/P. A. Studer	1
711.2/G. E. Rodriguez	1
712.0/K. Dolan	1
420.0/R. Volpe	1
Library	1
NASA Marshall Space Flight Center Marshall Space Flight Center, AL 38512	
Attn: JA51/Rein Ise	1
JA53/John Owens	1
JA52/Dwight Johnston	1
EB22/Paul Golley	1
ED15/Harry Buchanan	1
EE91/Harvey Shelton	1
EL54/Douglas Nixon	1
EL54/Robert Smith	1
AS24L/Library	1
Jet Propulsion Laboratory 4800 Oak Grove Drive Pasadena, CA 91103	
Attn: 198-112A/David Lehman	1
264-235/William Purdy	1
264-235/Ken Russ	1
T-1201/Edward Mettler	1
111-113/Library	1

DISTRIBUTION LIST (cont)

Address	Number of Copies
National Aeronautics and Space Administration Washington, DC 20546	
Attn: RC/Lee Holcomb	1
RC/Duncan McIver	1
RS/Leonard A. Harris	1
S/Richard F. Carlisle	1
S/John D. Hodge	1
United States Air Force Space Division P.O. Box 92960 Worldway Postal Center Los Angeles, CA 90009	
Attn: SD/YNSS/Major J. Bailey	1
SD/YNSS/Lt W. Possell	1
NASA Ames Research Center Moffett Field, CA 94035 Attn: Library, Mail Stop 202-3	1
NASA Dryden Flight Research Facility P.O. Box 273 Edwards, CA 93523 Attn: Library	1
NASA Lyndon B. Johnson Space Center 2101 Webster Seabrook Road Houston, TX 77058 Attn: JM2/Technical Library	1
NASA Lewis Research Center 21000 Brookpark Road Cleveland, OH 44135 Attn: 60-3/Library	1
NASA John F. Kennedy Space Center Kennedy Space Center, FL 32899 Attn: NWSI-D/Library	1
NASA Scientific and Technical Information Facility 6571 Elkridge Landing Road Linthicum Heights, MD 21090	15 plus original

NASA Contractor Report 172481

Impact of Magnetic Isolation on Pointing System Performance in the Presence of Structural Flexibility

J. Sellers

Sperry Corporation
Phoenix, Az 85036

Contract NAS1-16909,
Task Number 2
February 1985

NASA
National Aeronautics and
Space Administration

Langley Research Center
Hampton, Virginia 23665

SUMMARY

The Advanced Gimbal System (AGS) is an end-mount, three-axis gimballed pointing system designed for use in the Space Shuttle, while the Annular Suspension and Pointing System (ASPS) is an AGS with a six-degree-of-freedom magnetic system incorporated at the top of the gimballed pointing system. One major difference in the pointing performance of these two systems is that the AGS does not provide translational isolation; hence, at frequencies above its control bandwidth, base translational motion couples directly into payload pointing error. The ASPS, on the other hand, provides high-frequency attenuation (isolation) that is a function of the form bandwidth of the ASPS Vernier System (AVS) translational controllers.

Models of these two systems were developed from NASTRAN data, stabilized, and verified. Each was excited with a unity force input at the base of the pointing system, and a transfer function relating the output pointing angle to that input was developed. These two system responses were examined and their similarity to theoretical responses was noted. This agreement provided confidence that the models were indeed correct. The low-frequency asymptote of the ASPS response was 60 decibels lower than that of the AGS response, the major reason being that the AVS pointing loop is closed at a higher bandwidth than is the AGS elevation axis controller. Structural flexibility was the determining factor for the AGS controller bandwidth, while the ASPS stability was less affected by this flexibility. The Shuttle dynamics were then added to each model and the transient time response caused by a Shuttle VRCS jet firing was obtained. The peak value of the AGS disturbance response is 7.4 arc seconds, while that of the ASPS (obtained by correlating other system performance data) is approximately 0.007 arc second.

The use of magnetic suspension to separate the payload and pointing mount dynamics, as provided by the ASPS, reduces the detrimental effects of structural flexibility on the maximum achievable system controller bandwidth. Thus, with a high controller bandwidth, better disturbance rejection capability and pointing performance is achieved.

TABLE OF CONTENTS

LIST OF FIGURES

LIST OF TABLES

LIST OF ACRONYMS AND SYMBOLS

Coordinate Systems

X_O, Y_O, Z_O	Shuttle coordinate system axes
X,Y,Z	AGS-ASPS coordinate system axes

Acronyms

AGS	Advanced Gimbal System
ASPS	Annular Suspension and Pointing System
AVS	ASPS Vernier System
BMF	Bending Mode Filter
CDC	Control Dynamics Company
CG	Center of Gravity
CM	Center of Mass
DOF	Degree of Freedom
GSA	General Stability Analysis
HW	Hardware
IRU	Inertial Reference Unit
kip	kilopound
MBA	Magnetic Bearing Assembly
MJA	Mounting and Jettison Assembly
NASTRAN	NASA Structural Analysis
P-I-D	Proportional Plus Integral Plus Derivative
PMS	Payload Mounting Structure
PPA	Payload Plate Assembly
RPS	Radians per Second
SW	Software
VRCS	Vernier Reaction Control System

Symbols

B_i	Term proportional to damping of i^{th} mode (rad/sec)
e	Natural logarithm base (dimensionless)
η_i	i^{th} modal coordinate
η_i'	Component of η_i due to controller input
η_i''	Component of η_i due to disturbance input
F_{XT}	AVS force along X-axis (pounds)
F_{ZT}	AVS force along Z-axis (pounds)
J	Moment of inertia (slug-in^2 or slug-ft^2)
K_1	Spring stiffness in MJA model (kip/in.)
K_2	Spring stiffness in MJA model (kip/in.)
K_i	Square of i^{th} eigenvalue λ_i $(rad/sec)^2$
K_I	Integral gain in controller (rad/sec)
Kp	Proportional gain in controller (units vary)
ℓ_1	Payload CM offset in Z direction (inches)
ℓ_2	Distance between elevation gimbal axis and AVS actuator plane (inches)
ℓ_{MA}	Distance between shuttle CM and AGS base along shuttle roll axis (inches)
λ_i	Eigenvalue of i^{th} mode (rad/sec)
M	Mass (slugs)
ω_1	Break frequency of lead network (rad/sec)
ω_2	Break frequency of lag network (rad/sec)
$\phi_{i,j}$	j^{th} component of i^{th} eigenvector
Q	Quality factor (dimensionless)
R	GSA simulation data variable

LIST OF ACRONYMS AND SYMBOLS (cont)

S	Laplacian operator (rad/sec)
t_d	System time delay (seconds)
θ_g	AGS model output angle (radians)
θ_{gC}	AGS model command angle (radians)
θ_{gA}	AGS output angle in ASPS model (radians)
θ_{CMD}	AVS pointing loop command angle (radians)
θ_S	Shuttle small angle rotation about Y_o (radians)
θ_{YgP}	AVS pointing loop output angle (radians)
$T_{\theta P}$	AVS pointing loop torque command (in.-lb)
U	Generic system input vector
U_D	AGS base force input (pounds)
U_E	AGS elevation gimbal torque output (in.-lb)
X_{gA}	AGS node 9 X-displacement in ASPS model (inches)
X_{gP}	AVS node 9 X-displacement in ASPS model (inches)
Z_{gA}	AGS node 9 Z-displacement in ASPS model (inches)
Z_{gP}	AVS node 9 Z-displacement in ASPS model (inches)
ξ_i	Damping factor associated with i^{th} mode (dimensionless)

ABSTRACT

A study has been conducted to compare the inertial pointing stability of a gimbal pointing system, the AGS, with that of a magnetic pointing and gimbal follow-up system, the ASPS, under certain conditions of system structural flexibility and disturbance inputs from the gimbal support structure. Separate three-degree-of-freedom (3DOF) linear models, based on NASTRAN modal flexibility data for the gimbal and support structures, were generated for the AGS and ASPS configurations. Using the models, inertial pointing control loops providing more than 6 decibels of gain margin and more than 45 degrees of phase margin were defined for each configuration. The pointing-loop bandwidth obtained for the ASPS is more than twice the level achieved for the AGS configuration. The AGS limit can be directly attributed to the gimbal and support structure flexibility. As a result of the higher ASPS pointing-loop bandwidth and the disturbance rejection provided by the magnetic isolation, ASPS pointing performance is significantly better than that of the AGS system. Specifically, the low-frequency (non-modal) peak of the ASPS transfer function from base disturbance to payload angular motion is almost 60 decibels lower than the AGS low-frequency peak.

INTRODUCTION

In the last decade, firm definition has emerged for many of the payloads to be flown on various Shuttle missions. Characteristics of several types of these payloads clearly dictate the need for sub-arc second pointing stability in the presence of undesired system disturbances, such as astronaut motion and Shuttle VRCS jet firings. In the classical sense of control system theory, one could simply increase the bandwidth of the payload pointing system controller(s) until the desired disturbance rejection capability is achieved, while, of course, maintaining a stable system. This stipulation places an upper bound on the disturbance rejection capability of such a system from a purely theoretical standpoint. When using a system such as the Advanced Gimbal System (AGS), a high controller bandwidth is desired for the purposes of disturbance rejection;

however, no translational disturbance rejection can be achieved at frequencies above the controller bandwidth. One major reason for this lies in the fact that the AGS provides a solid link - a moment arm - between the Shuttle-AGS base interface and the payload. Thus, high-frequency base vibration can and will transmit directly to the payload, and the system controller(s) can do little in the way of attenuating or rejecting such a disturbance.

Another major system characteristic that will impact the maximum allowable bandwidth of the system is the structural flexibility of the system itself. This flexibility encompasses bending modes whose frequencies are a function of the stiffness of the supporting structure, the lengths of the individual structural components, and the size of the supported payload itself. These modes present themselves, in the frequency domain, as highly underdamped poles whose amplitude depends upon the damping factor (usually assumed) associated with that particular mode, and, in the time domain, as ringing effects whose frequency of oscillation is the modal frequency. In addition, when considering system stability, the peaking associated with a bending mode will usually force the reduction of the system bandwidth. This fact is due to the gain-phase characteristics of the mode at frequencies which are very close to the modal frequency. At these frequencies, the gain is higher than is the rigid-body response; however, the phase drops off and reverses by 180 degrees as the frequency of interest approaches and then exceeds the modal frequency. In other words, if the open-loop crossover frequency is sufficiently close to the modal frequency, the phase drop associated with the mode will decrease the available phase margin at the crossover. This detrimental result forces a decrease in the value of the open-loop crossover frequency, which further reduces the closed-loop bandwidth.

The payload size and the length and stiffness of the members of the supporting structure play a large role in determining the values of the modal frequencies. Assuming a constant stiffness value for these members, increasing their lengths will decrease the modal frequencies. Furthermore, assuming a constant stiffness and length for each member, increasing the payload mass/

inertia will also decrease the modal frequencies. It can, therefore, be seen that the AGS structure and payload characteristics are important in determining the modal frequencies and, consequently, the system bandwidth.

Several plausible alternatives exist which will reduce, to a certain extent, the determental effects of structural flexibility on pointing performance. One solution is to manufacture the structure from a stiffer material which will tend to increase the modal frequencies. The drawbacks associated with this method are the additional expense and also the fact that there is still no translational disturbance rejection capability at frequencies above the controller bandwidth. Another solution is to include a bending mode filter (BMF) as part of the control law; however, this more refined controller does not cure all of the flexibility problems. The disadvantages associated with this method are: 1) the location of the modal frequencies is not precisely known and the structural damping can only be assumed, leaving a degree of inaccuracy in the control law; 2) the coefficients of the BMF are only accurate at the system attitudes for which structural data are available, forcing the use of a digitally-implemented tracking algorithm in a gimballed system where bending mode frequencies and shapes vary with the gimbal angle; and 3) there will still be no translational disturbance rejection capability at frequencies above the controller bandwidth. Another alternative is to use a system such as the ASPS Vernier System (AVS) in conjunction with the AGS to form a pointing and isolation system, the Annular Suspension and pointing System (ASPS). Figures 1 and 2 illustrate the major features of the AGS and ASPS, respectively.

The AVS is a six-degree-of-freedeom pointing system composed of two noncontacting sections - a stator and an armature. The stator is rigidly attached to the top-mounting structure of the AGS, and the payload is attached to the armature. Six magnetic bearing assemblies (MBA) provide active control over the six degrees of freedom of the levitated payload. The control law associated with each axis can be independently implemented. Coupling between translation and rotation is significantly reduced in the AVS through a unique decoupling scheme incorporated into the system design (ref 1). The AVS, most importantly, can attenuate high-frequency translational effects due to the soft interface between the armature and stator.

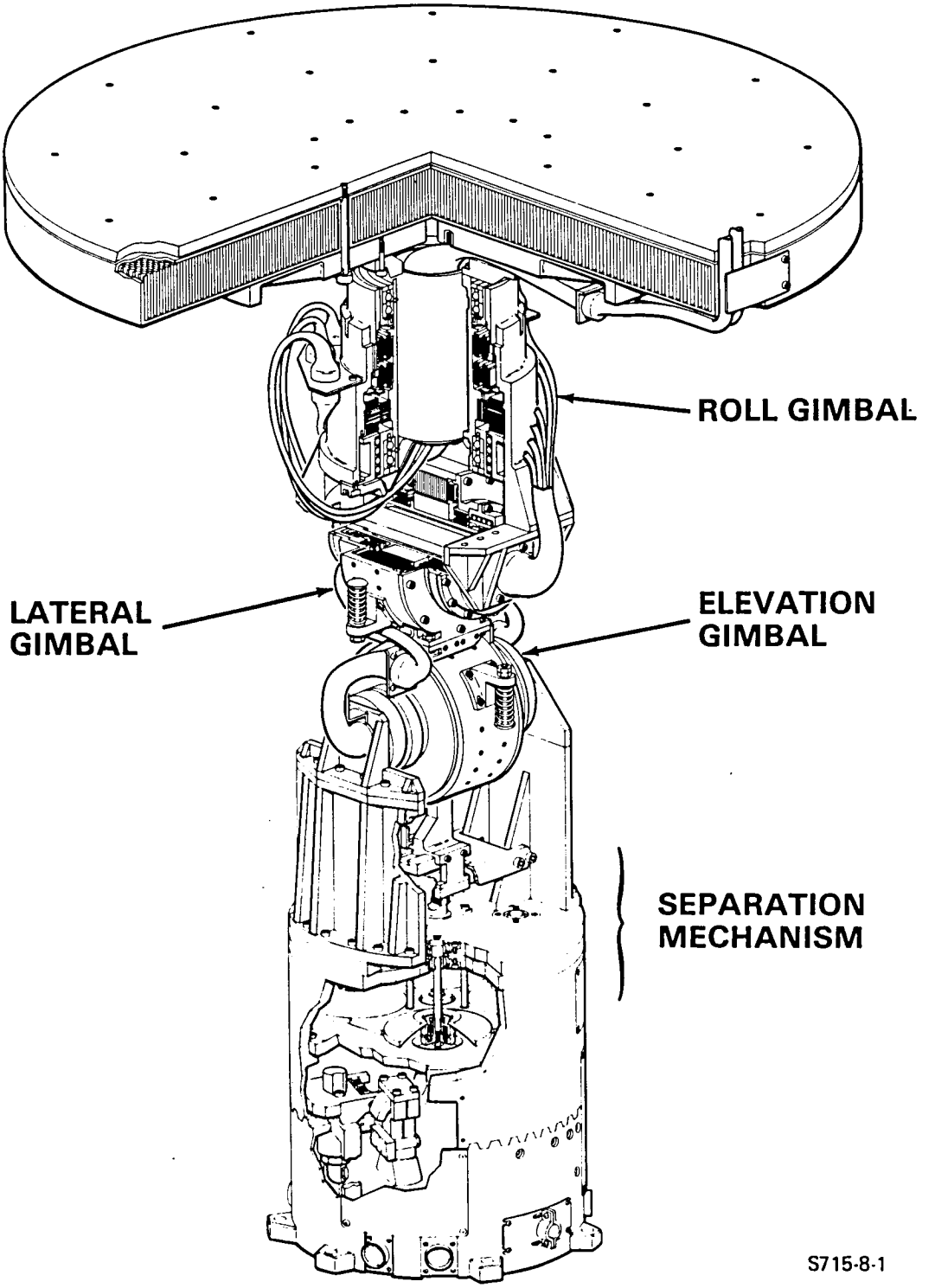

Figure 1
Advanced Gimbal System (AGS)

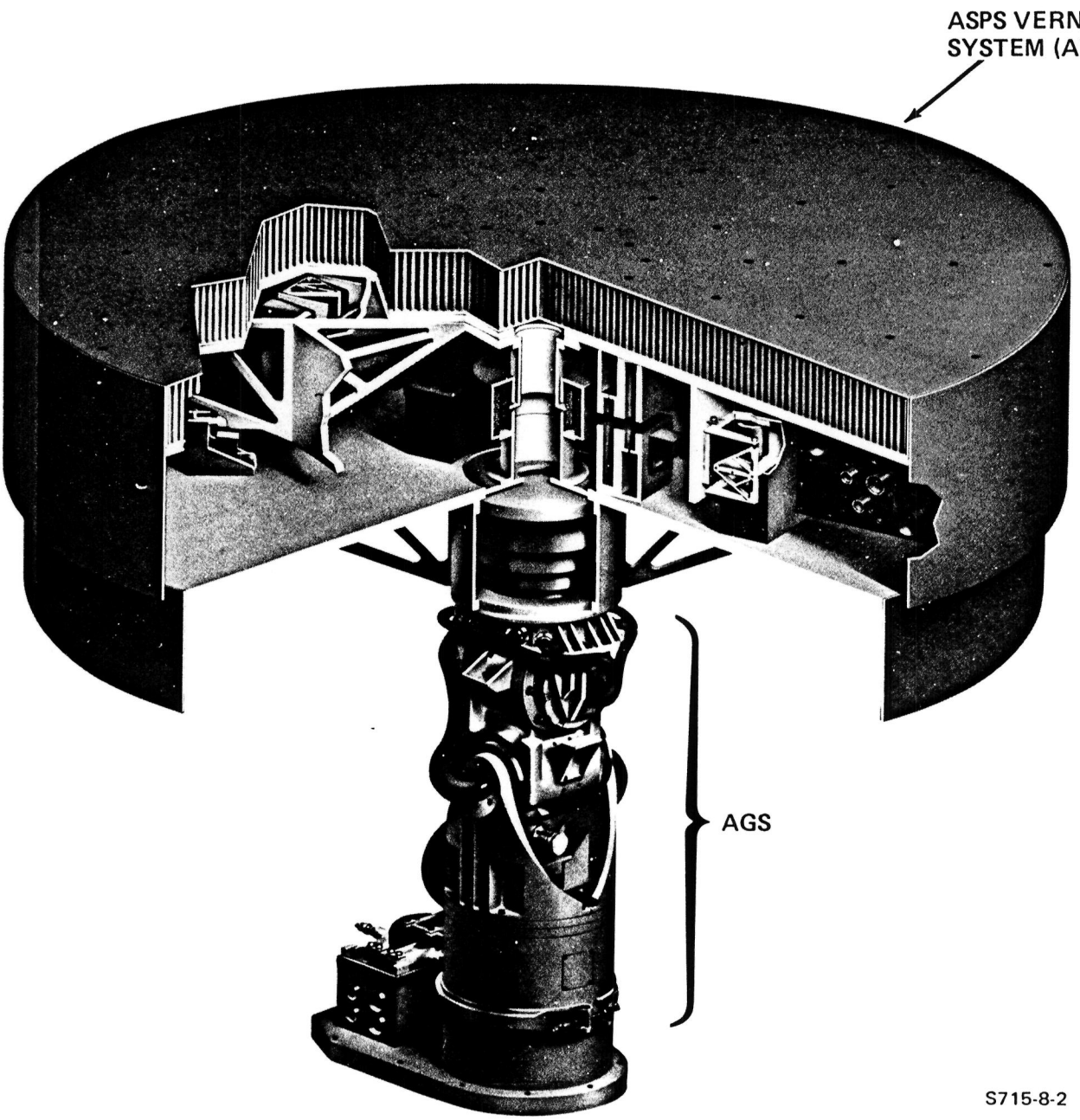

Figure 2
Annular Suspension and Pointing System (ASPS)

The previous discussion has emphasized the effects of the structural flexibility of the AGS on payload pointing performance. However, when the AVS is used in conjunction with the AGS, the structural flexibility of the armature/payload assembly has to be considered in addition to that of the AGS. This is due to the nature of the AVS translational and rotational control laws. The AVS translational controllers are designed to keep the armature/payload centered in the magnetic bearing gaps. However, if the armature/payload assembly flexes, this motion is also sensed by the translation controller. Therefore, payload flexibility couples into the translational control and hence into the AVS pointing system dynamics.

In this section, an attempt has been made to give a qualitative explanation of the effects of structural flexibility on the pointing performance of the AGS and the ASPS. In the following sections, NASTRAN data will be used to develop planar models of the AGS and the ASPS. These models will then be used to evaluate the merits and performance of each system in the presence of a disturbance environment.

DEVELOPMENT OF FLEXIBILITY MODELS

This section is concerned with the development of the linear system models to be used in the study and analysis of the effects of structural flexibility on the pointing performance of the AGS and the ASPS. The approach taken will be to use rigid link "stick" models with compliant interfaces to characterize the AGS structure. The mounting structure between the base of the AGS and the Shuttle is modeled by a mass-double spring arrangement shown as Figure 6.3.14 in a Control Dynamics Company (CDC) study done for the NASA Marshall Space Flight Center and Sperry Flight Systems in March, 1982 (ref 2). This response is redrawn in Figure 3 for reference. A Bode plot of the mass-double spring model response is also shown in Figure 3. A frequency domain expression that can be used to approximate the mass-double spring response is as follows:

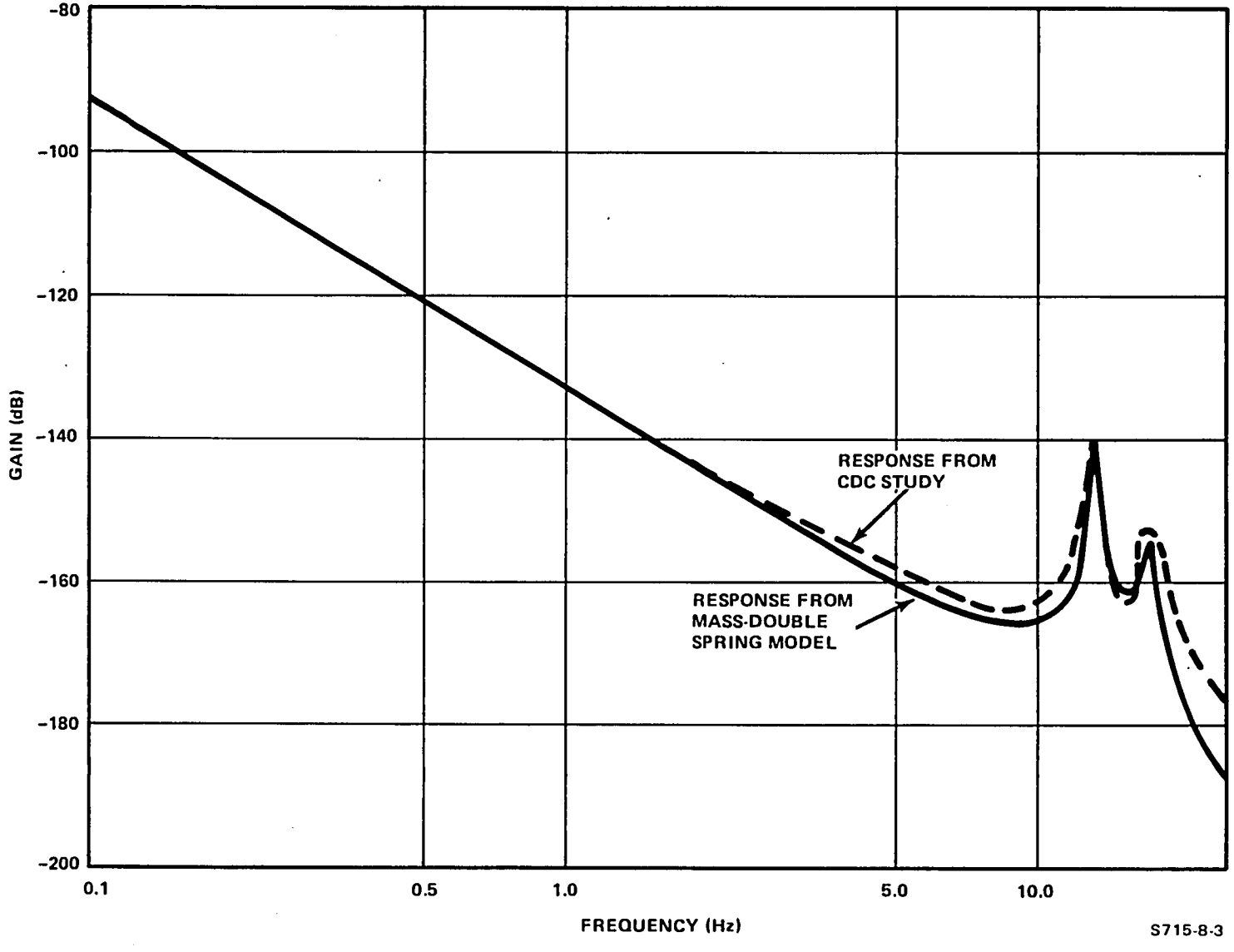

Figure 3
Open-Loop Transfer Function Relating Output
Pointing Angle to Applied Elevation Gimbal Torque

$$\frac{8.78 \times 10^{-6}}{S^2} - \frac{1.316 \times 10^{-5}}{S^2 + 1.75S + 6906} + \frac{1.038 \times 10^{-5}}{S^2 + 5.5S + 11881}$$

The Q of the first flexible mode is equal to 40, while that of the second mode is 20. As can be seen from this expression, the two flexible modes are superimposed on top of the rigid-body response which is $1/Js^2$. Also, by comparing Figure 3 of this report with Figure 6.3.14 of reference 2, it can be seen that the first two modal frequencies, as well as the peaks, are in good agreement.

The payload used in both system studies is a flexible, 20-hertz body, meaning that, if such a body were to be used as a cantilevered beam and then struck, the frequency of oscillation would be 20 hertz. For the AGS model, this payload is rigidly attached to the supporting structure (free-fixed); for the ASPS, the payload/AVS armature body is suspended above the AGS-AVS stator body (free-free). Thus, for the ASPS model, two sets of modal data are required - one for each separate body.

The above discussion merely provides a brief description of the hardware and system plants. In the next two subsections, planar models of each system will be developed, structural data in modal form (obtained from NASTRAN runs) will be used to develop a plant model of each, and system block diagrams which incorporate these plant models will be developed.

Development of Flexible AGS Model

The AGS utilizes three gimbals to provide three-degree-of-freedom payload motion, one about each gimbal axis. However, for the purposes of this study, the motion will be restricted to a single-degree-of-freedom rigid-body rotation about the AGS y-axis (elevation gimbal axis) in the X-Z plane. Such a model is simpler to analyze than a complete three-degree-of-freedom model, yet will nevertheless yield useful, relevant results.

A planar model of the AGS-payload configuration is shown in Figure 4. The pertinent links to be used in the model are as labeled on the figure. As stated earlier, the MJA is modeled by a mass-double spring. The spring denoted by K_1 has a stiffness of 40 kilopounds per inch, while the spring constant K_2 of the second spring is 160 kilopounds per inch. The mass M is a 12-slug mass. For frequency responses, the system input is a force of unity value at node 11. For time-response runs, the input is a VRCS pulse that is applied to the Shuttle (node 12). It is desired to determine how Shuttle motion affects the motion of the mass M.

The first step in the solution of this problem is to determine how forces and torques at the Shuttle Center of Mass (CM) create AGS base motion. A drawing of the Shuttle, which locates its CM relative to the envelope of the payload bay, is shown in Figure 5. The Shuttle axes are as shown on the figure, with the axis Y_0 completing a right-hand system. It is necessary to determine the distance between the Shuttle CM and the AGS base along the Shuttle roll axis X_0. Assuming that the AGS is mounted 17.5 feet behind the front portion of the payload bay, with the elevation gimbal axis being parallel to the Shuttle roll axis, then using the dimensions on Figure 5, the desired moment arm length is [1147 - (682 + 17.5 x 12)] inches, or 255 inches. This distance is defined as ℓ_{MA}. It is recognized that, normally, the elevation axis is transverse to the Shuttle roll axis. However, since AGS NASTRAN data are available only at the (0,0,0) degrees gimbal attitude, a Shuttle pitch maneuver (used in other studies) would not produce an AGS pointing disturbance. Thus, for this study, the elevation gimbal axis will be considered to be parallel to the Shuttle roll axis. Now, if a VCRS yaw maneuver (small angle rotation about Z_0) is performed and defined as θ_S, the AGS base displacement along the Shuttle Y_0 axis is $| \ell_{MA}\theta_S |$ inches. This base displacement shoves against the 12-slug mass in Figure 4 by compressing the spring whose stiffness is K_2, in turn exciting the flexible AGS structure. Since Shuttle motion in this direction would cause the AGS to tip about the elevation gimbal axis, the gimbal controller would try to correct this error. Thus, the dynamics of the Shuttle-pallet-AGS interfaces that cause AGS flexible-body motion have been described and will be used in both the AGS and ASPS model development. It is now necessary to describe the AGS

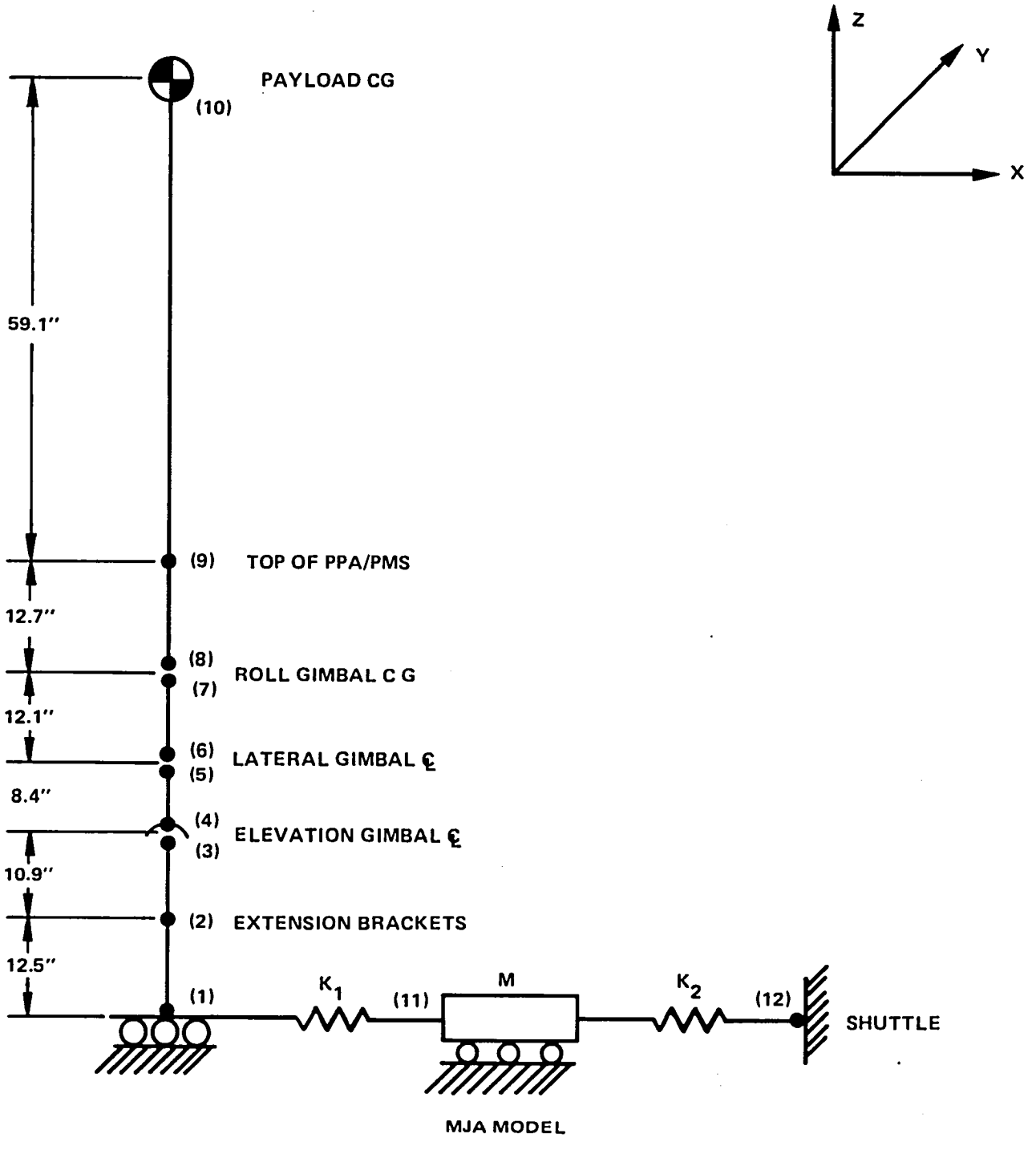

Figure 4
Planar Model of AGS-Payload Configuration

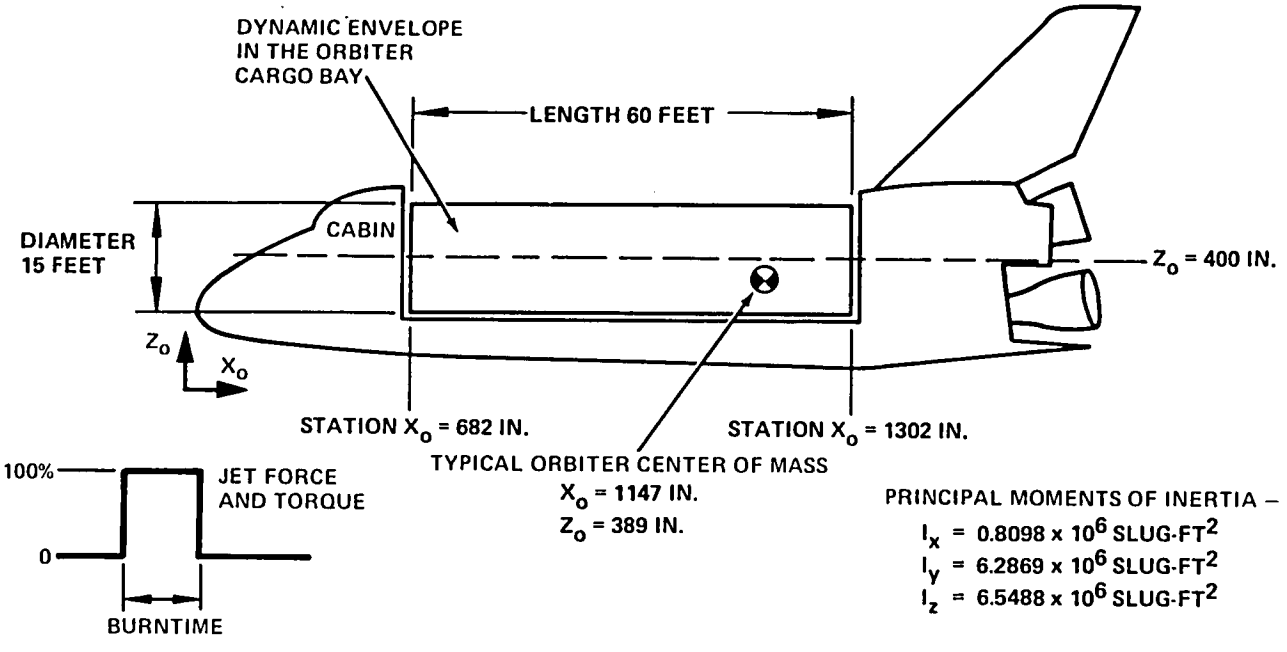

VRCS AXIS	BURN TIME (SEC)	PEAK FORCES AND TORQUES					
		F_x (LB)	F_y (LB)	F_z (LB)	T_x (FT-LB)	T_y (FT-LB)	T_z (FT-LB)
ROLL	0.24	0	-41.42	44.12	504.0	0	0
PITCH	0.24	0	0	50.1	0	-1830.5	0
YAW	0.24	0	8.6	19.1	0	0	1914.7

MASS = 5794.1 SLUGS

S715-8-5

Figure 5
Shuttle Center-of-Mass Location and Payload Bay Location

plant in modal coordinate form and to use the resulting model as the plant in an overall AGS system model.

For this particular study, the AGS plant will be described by one rigid-body mode (single-degree-of-freedom) and two prominent flexible-body modes. The outputs of these three modal paths are summed together to form the total flexible-body motion. Such a representation can be viewed as being a partial fraction expansion of the plant transfer function, which means that the fidelity of the model can always be increased by appending additional modal dynamics in parallel with the existing ones. Also, an important point to be made is that, due to the parallel structure, one modal output can and will excite all other system modes through the feedback control law.

The modal equations that describe the AGS flexible-body motion are of the form

$$[S^2 + B_i\ S + K_i]\ \eta_i = [\phi_i]^T\ \overline{U} \qquad (1)$$

where B_i is related to the damping associated with the i^{th} mode, K_i is the square of the i^{th} eigenvalue λ_i, ϕ_i is the i^{th} eigenvector associated with λ_i, and $\overline{U}$ is the system input vector. The variable η_i is the modal coordinate associated with the i^{th} mode. The right-hand side of equation (1) describes how the various modes are excited by the input $\overline{U}$. The i^{th} eigenvector contains N components, where N is equal to the number of nodes in the model multiplied by the degrees of freedom. Since this is a planar analysis, each node has three degrees of freedom; X, Z, and θ; NASTRAN outputs are in that order at each node. Thus, for the AGS, the eigenvector for each mode has 33 elements (11 nodes times 3DOF).

For this model, the desired system input is the single-degree-of-freedom, rigid-body rotation about the elevation gimbal axis. By studying Figure 4, it can be seen that this input would be applied as $+U_E$ at node 4, while the reaction torque on the structure due to this input would be applied as $-U_E$ at

node 3. Using these facts and equation (1), the equation for the desired response portion (η_i') for the i^{th} modal coordinate η_i is

$$\eta_i' = \frac{(\phi_{i,26} - \phi_{i,25})\ U_E}{S^2 + B_i\ S + K_i} \tag{2}$$

To complete the structural model, the response of the system to an undesired base input (U_D) must be included. Again, by using Figure 4 as a reference, the base disturbance input U_D will be applied at node 11 in the X direction; thus, the equation for the disturbance response portion (η_i'') of the same i^{th} modal coordinate is

$$\eta_i'' = \frac{\phi_{i,11}\ U_D}{S^2 + B_i\ S + K_i} \tag{3}$$

The i^{th} modal coordinate η_i is the sum of the two components given by equations (2) and (3) and is

$$\eta_i = \eta_i' + \eta_i'' \tag{4}$$

The rotational motion of node 9 is the output of interest (inertial reference unit is located at this point) and is given by the expression

$$\theta_9 = \Sigma\phi_{i,9}\ \eta_i \quad ; \quad i = 1,2,3 \tag{5}$$

This angle is sensed by the inertial reference unit (IRU), fed back, and is compared to the commanded angle θ_C. The resulting error signal is then used by the system controller to produce the desired system command. In equation form,

$$U_E = G(s)\ [\theta_{9C} - \theta_9] \tag{6}$$

where U_E is as used in equation (2); and G(s) is a cascaded combination of the elevation gimbal controller $G_E(s)$, a bending mode filter (BMF), and a Pade time-delay expression (to account for the phase-lag effects caused by the digital implementation of the control law).

A system block diagram that incorporates all of the previous discussion and derivations is shown in Figures 6a and 6b. A listing of the numerical values used in the structural portion of this model is given in Table I. The form of G(s) will not be defined here, but will be defined in the next major section. In the following subsection a similar model will be developed for the ASPS. It is worth mentioning, at this point in the discussion, that the symbology used in the ASPS model development will be the same as that used in the AGS case; however, the subscripts and numerical values used will be different.

Development of Flexible ASPS Model

The model of the flexible ASPS will be developed by using the same methodology as that used in the formulation of the AGS model. The MJA model (whose dynamics are described by the expression on page 15) is the same, as is the addition of the Shuttle dynamics. The same 20-hertz payload is also used; however, it is not physically detached from the rest of the system and is a free-free body (as opposed to a free-fixed body in the AGS case).

A planar model of the ASPS-payload configuration is shown in Figure 7. As before, the pertinent links and nodes are defined per the figure. Note the magnetic interface, and note also that nodes 9P, 10P, and 10 are used in the figure. The AGS-AVS stator motion is constrained to the same rigid-body rotational degree of freedom about the elevation gimbal axis, while the AVS armature motion is constrained to three rigid-body degrees of freedom: translational motion along the X and Z axes and rotational motion (θp) about the Y-axis. Therefore, for this model, the AGS-AVS stator will be described by a single rigid-body mode and two priminent flexible-body modes while the AVS armature body will be characterized by three rigid-body modes (one for each degree of freedom) and two priminent flexible-body modes. As an aside, the eigenvectors and eigenvalues associated with the AGS subsystem will differ from those used in the AGS-payload model, due to the fact that the two bodies are not physically attached in the ASPS. The eigenvector associated with each payload mode has six elements (two nodes and three degrees of freedom), while the

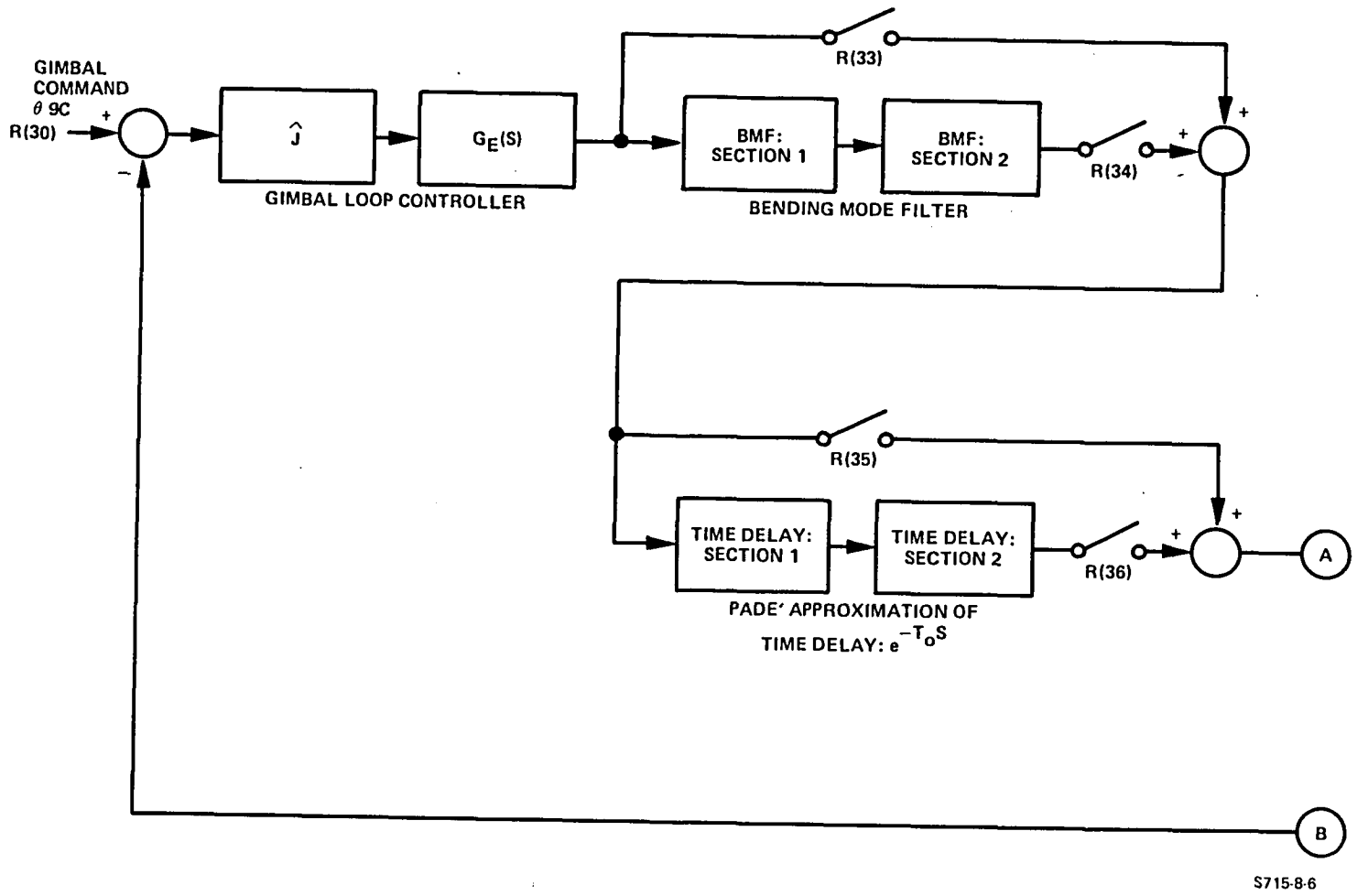

Figure 6a
AGS Block Diagram

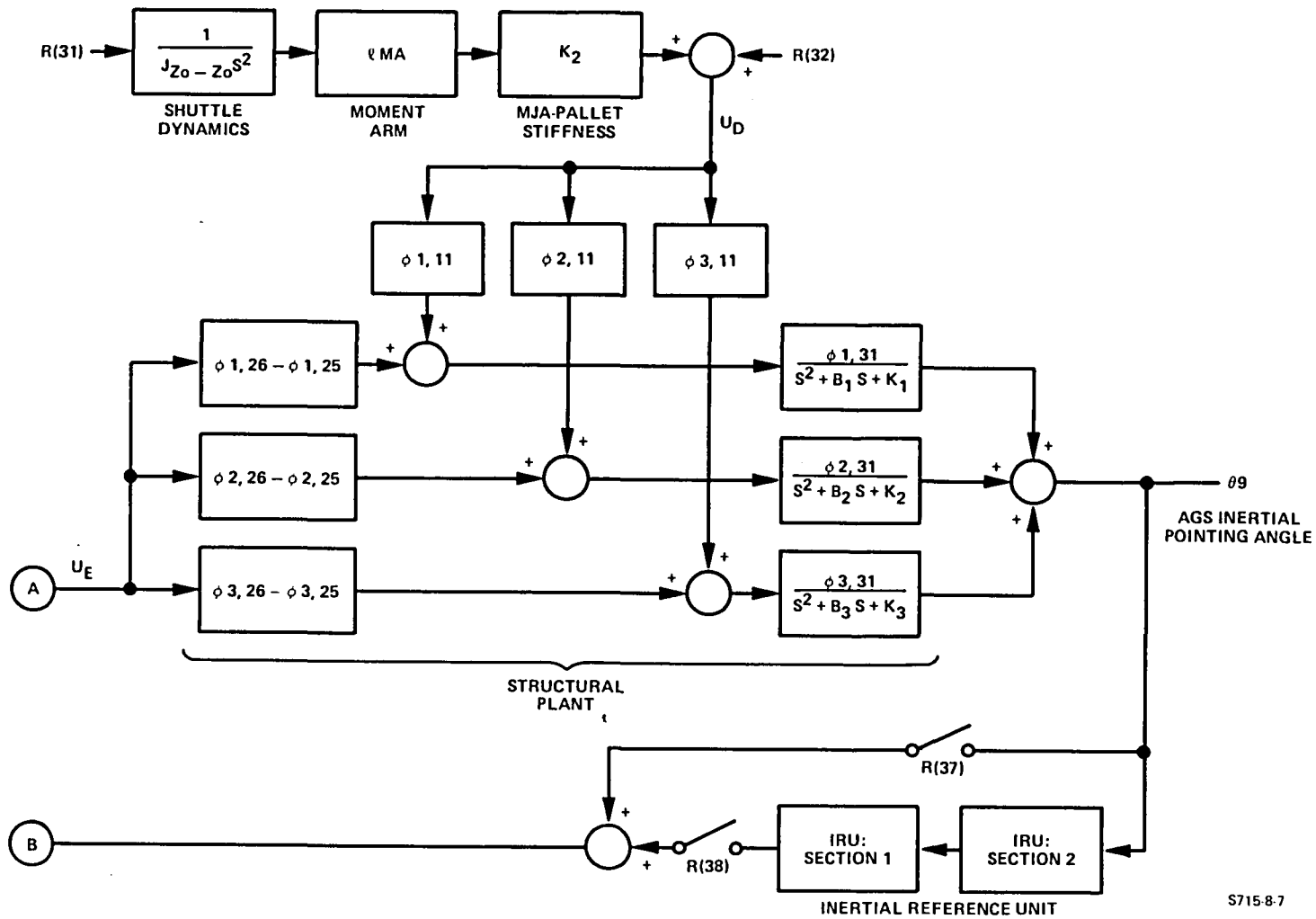

Figure 6b
AGS Block Diagram (cont)

TABLE I

NUMERICAL VALUES USED IN THE AGS STRUCTURAL MODEL
(Obtained from NASTRAN)

Rigid-body mode: $i = 1$

$\xi_1 = 0.0$ $\lambda_1 = 0.0$

$B_1 = 0.0$ $K_1 = 0.0$

$\phi_{1,11} = 0.0$

$\phi_{1,25} = 0.0$

$\phi_{1,26} = 2.921244 \times 10^{-3}$

$\phi_{1,31} = 2.921244 \times 10^{-3}$

First flexible-body mode: $i = 2$

$\xi_2 = 0.005$ $\lambda_2 = 73.587$

$B_2 = 0.736$ $K_2 = 5415$

$\phi_{2,11} = -0.1167225$

$\phi_{2,25} = 0.0$

$\phi_{2,26} = -3.372369 \times 10^{-3}$

$\phi_{2,31} = 4.210238 \times 10^{-3}$

Second flexible-body mode: $i = 3$

$\xi_3 = 0.005$ $\lambda_3 = 113.94$

$B_3 = 1.1394$ $K_3 = 12983$

$\phi_{3,11} = -0.2201011$

$\phi_{3,25} = 0.0$

$\phi_{3,26} = 8.189604 \times 10^{-3}$

$\phi_{3,31} = -1.795968 \times 10^{-3}$

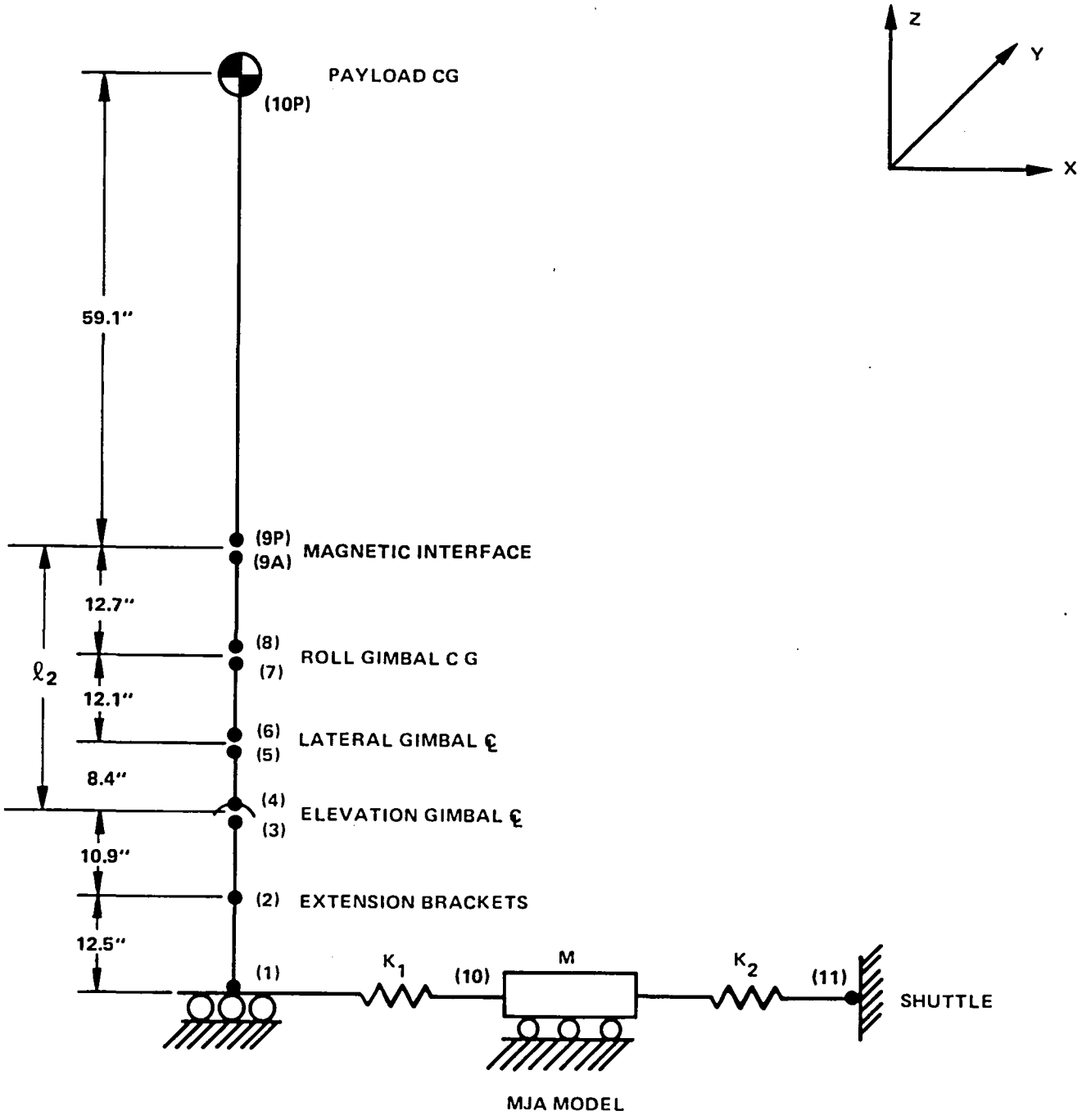

Figure 7
Planar Model of ASPS Configuration

eigenvector associated with each AGS-mounting structure mode has 30 elements (ten nodes, each with three degrees of freedom). The base disturbance input is at node 10 in this model and the Shuttle is node 11.

The modal equations that describe the AVS armature/payload flexible-body motion are of the form

$$[S^2 + B_i\ S + K_i]\ \eta_i = [\phi_i]^T\ \overline{U} \qquad i = 1,2...5 \tag{7}$$

where the modal coordinate η_i, damping B_i, stiffness K_i, and eigenvector ϕ_i have the same generic meaning as in the AGS case and the vector $\overline{U}$ is the input vector (controller outputs) to the payload body. This vector is of the form.

$$\overline{U} = \begin{bmatrix} F_{XT} \\ F_{ZT} \\ T_{\theta P} \end{bmatrix} \tag{8}$$

and is applied at the base (node 9P) of this body. As before, the right side of equation (7) describes how the various payload modes are excited by this input. For the payload model, the eigenvector for each mode contains six elements (two nodes and three degrees of freedom) and describes the motion at the payload base as well as its CM.

Using these facts and equations (7) and (8), the modal equations for the motion of the payload are

$$[S^2 + B_i\ S + K_i]\ \eta_i = \tag{9}$$

$$[\phi_{i,1}\ F_{XT} + \phi_{i,3}\ F_{ZT} + \phi_{i,5}\ T_{\theta P}] \qquad i = 1,2...5$$

These equations describe how the various payload modes are excited by the AVS controller output commands. The total payload motion in the X, Z, and θ directions is given by the following expressions:

$$X_{9P} = \Sigma\, \phi_{i,1}\, \eta_i \qquad i = 1,2...5 \qquad (10a)$$

$$Z_{9P} = \Sigma\, \phi_{i,3}\, \eta_i \qquad i = 1,2...5 \qquad (10b)$$

$$\theta_{Y9P} = \Sigma\, \phi_{i,5}\, \eta_i \qquad i = 1,2...5 \qquad (10c)$$

These quantities are the actual positions of the base of the payload (node 9P) and are compared to either an inertial command angle (θ_{CMD}) or to the X and Z translational motions, defined as X_{9A} and Z_{9A}, respectively, on the AGS side of the magnetic interface. The resulting error signals, defined as the difference between respective motions, are sensed and used by dynamic controllers to produce the required translational and rotational motion commands. In equation form these relationships are:

$$F_{XT} = G_X(S)\,[X_{9A} - X_{9P}] \qquad (11a)$$

$$F_{ZT} = G_Z(S)\,[Z_{9A} - Z_{9P}] \qquad (11b)$$

$$T_{\theta P} = G_\theta(S)\,[\theta_{CMD} - \theta_{Y9P}] + \ell_1\, F_{XT} \qquad (11c)$$

where the control torque $\ell_1\, F_{XT}$ is a control law implementation and is required to counter the overturning moment produced when x-translaltional motion at the payload base couples into payload rotation. The distance ℓ_1 is the distance between the plane of the magnetic actuators and the effective payload CM location along the Z-axis and is known as the CM offset.

At this point in the discussion, the entire AVS armature/payload body has been characterized. The next task in the ASPS model development is to determine the modal coordinate representation of the AGS and its interfaces to the AVS. The approach taken will be basically the same as before (same number and types of modes, etc), but during the ASPS operation, the AGS is in a follow-up mode to the AVS; and the AVS armature/payload body will exert reaction forces and torques on the AGS-AVS stator as it moves in the magnetic gap. All other operations and equation forms are similar in nature to previously derived relations and will just be stated.

The flexible body motions at node 9 of the AGS side of the magnetic interface are given by

$$X_{9A} = \Sigma\ \phi_{i,9}\ \eta_i \tag{12a}$$

$$Z_{9A} = \Sigma\ \phi_{i,19}\ \eta_i \qquad i = 1,2,3 \tag{12b}$$

$$\theta_{9A} = \Sigma\ \phi_{i,29}\ \eta_i \tag{12c}$$

and are derived in a similar fashion as equations (10a) to (10c). The modal coordinates η_i are derived like those in equations (2) to (4), but for this model, the base disturbance input is at node 10 and the gimbal input is at nodes 3 and 4. In addition the AVS motion exerts reaction forces and torques on the AGS at node 9. Therefore, the complete expression for the i^{th} AGS modal coordinate η_i is

$$\eta_i = \frac{(\phi_{i,24} - \phi_{i,23})\ U_E}{S^2 + B_i\ S + K_i} + \frac{\phi_{i,10}\ U_D}{S^2 + B_i\ S + K_i} - \frac{\phi_{i,9}\ F_{XT}}{S^2 + B_i\ S + K_i}$$

$$- \frac{\phi_{i,19}\ F_{ZT}}{S^2 + B_i\ S + K_i} - \frac{\phi_{i,29}\ T_{\theta P}}{S^2 + B_i\ S + K_i} \qquad i = 1,2,3 \tag{13}$$

In equation (13), the variable U_E is the AGS follow-up mode controller output, U_D is the AGS base motion, and F_{XT}, F_{ZT}, and $T_{\theta P}$ are as defined by equation (11).

The controller output U_E is composed of three components: the AGS follow-up mode controller output and two feed-forward commands from the AVS, which are used to counter the reaction forces and torque caused by the AVS shoving against the AGS. The AVS pointing loop torque command $T_{\theta P}$, whose expression is given by equation (11c), is fed forward to the AGS controller, as is the torque produced by the AVS translational force F_{XT}, given by equation (11a), acting through the moment arm ℓ_2 as defined by Figure 7. Thus, the equation for the follow-up mode controller output U_E is

$$U_E = G_{FUM}(S)\ (\theta_{Y9P} - \theta_{9A}) + T_{\theta P} + \ell_2\ F_{XT} \qquad (14)$$

where $G_{FUM}(s)$ is the AGS follow-up mode controller (explicitly defined in a later section), and the other terms are as previously defined.

A block diagram that incorporates the previous discussion and equations (7) through (14) is shown in Figures 8a and 8b. As can be seen from these figures, the payload angle θ_{Y9P} (obtained from a gap transformation matrix) is the input to the AGS follow-up mode controller, while the same angle is sensed by an IRU and used as the feedback in the AVS pointing loop. Another very noticeable feature seen on this diagram is the parallel path structure associated with each flexible body. As in the AGS case, each modal output can excite every other mode in the system through the feedback control laws. A listing of the numerical values used in the structural portions of this modal is given in Table II.

In this section, the models for the flexible AGS and ASPS have been derived. These models are set up for simulation purposes as they are shown. In the next section, controllers will be designed, simulations of each model will be developed, and system performance analyses using these models and simulations will be conducted.

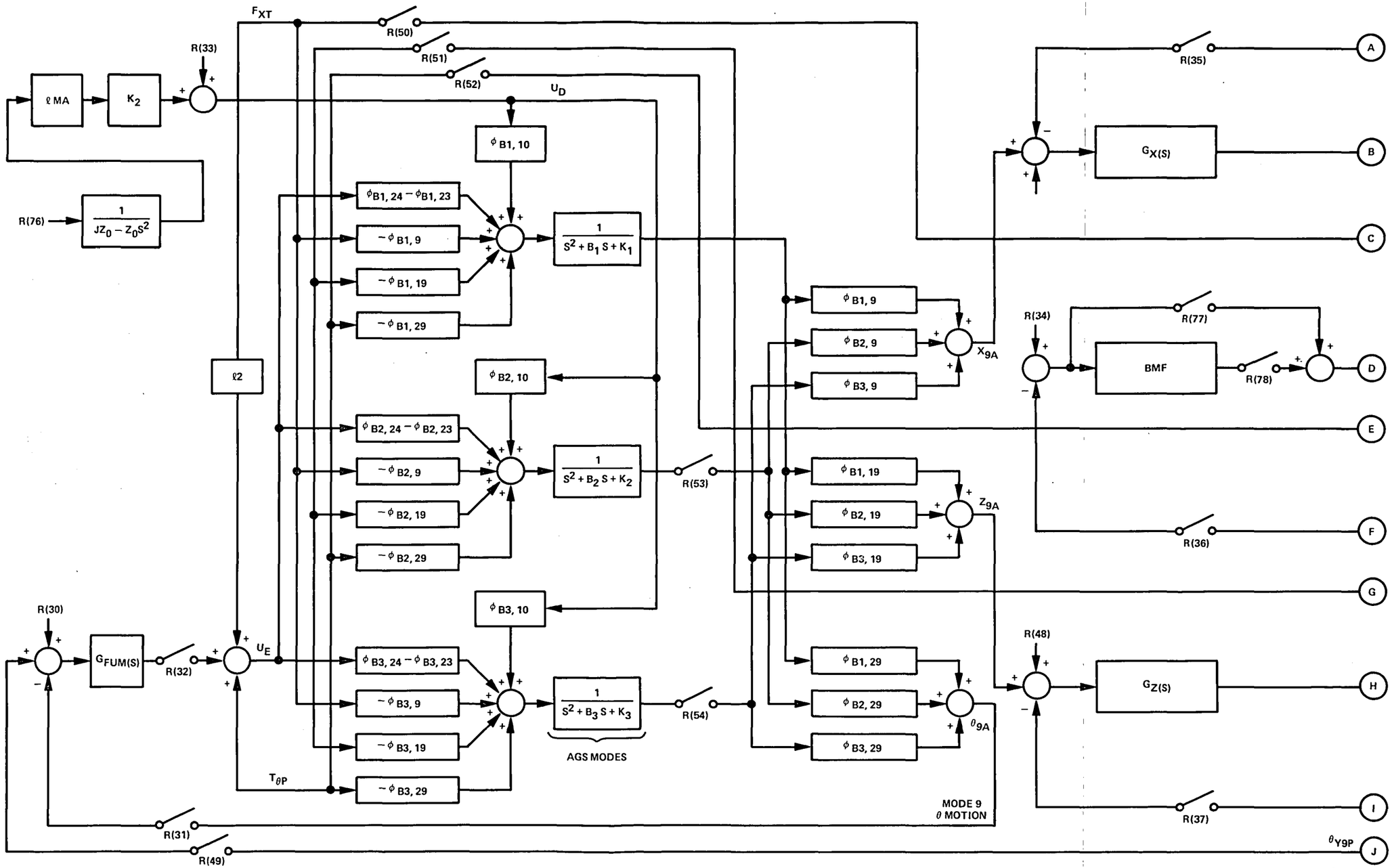

Figure 8a
ASPS Block Diagram

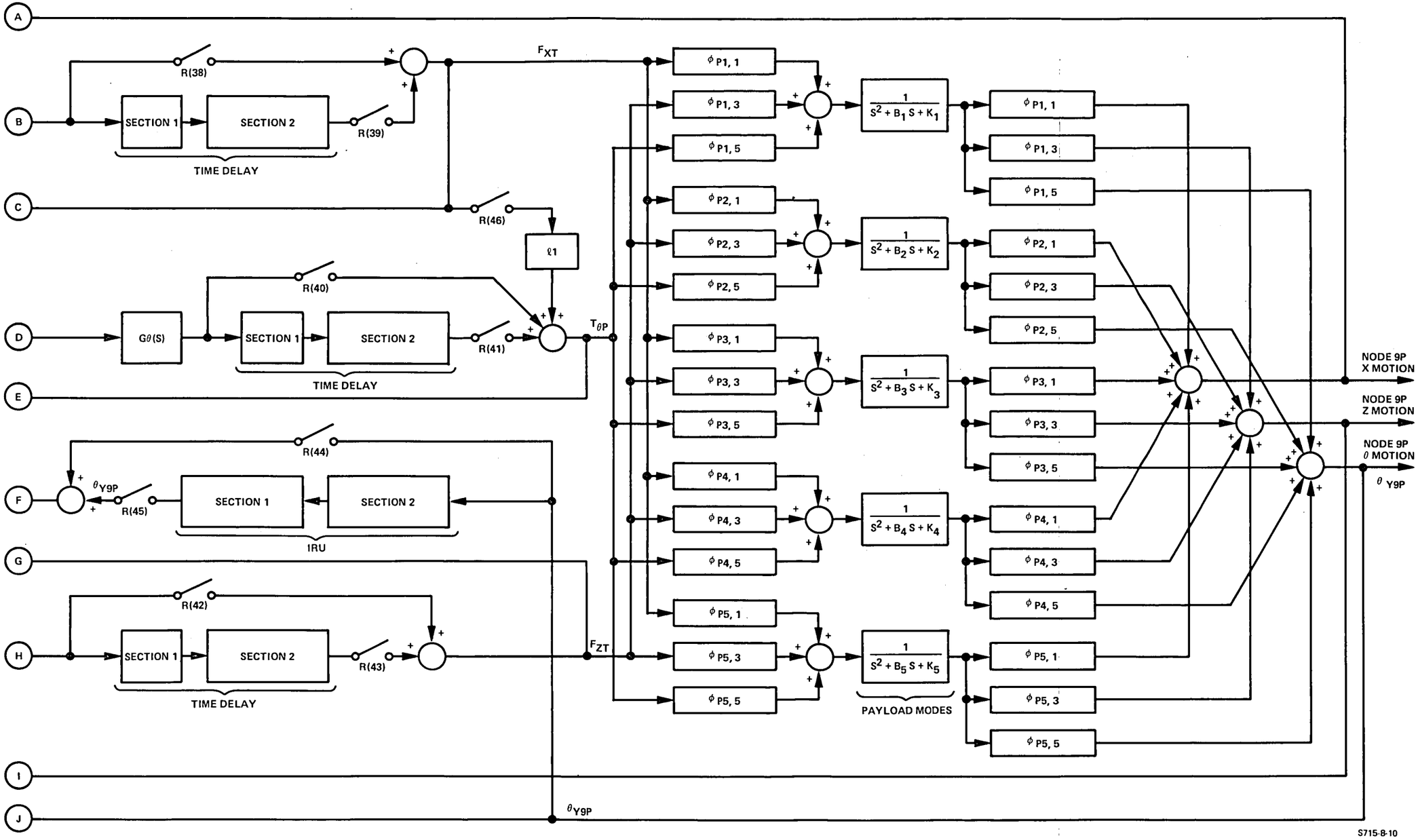

Figure 8b
ASPS Block Diagram (cont)

TABLE II

NUMBERICAL VALUES USED IN THE ASPS STRUCTURAL MODEL
(Obtained from NASTRAN)

AGS/AVS Stator: Rigid-body mode: i = 1

$\xi_1 = 0.0$ $\lambda_1 = 0.0$

$B_1 = 0.0$ $K_1 = 0.0$

$\phi_{1,10} = 0.0$

$\phi_{1,23} = 0.0$

$\phi_{1,24} = 2.954426 \times 10^{-2}$

$\phi_{1,29} = 2.954426 \times 10^{-2}$

First flexible-body mode: i = 2

$\xi_2 = 0.005$ $\lambda_2 = 97.64$

$B_2 = 0.976$ $K_2 = 9533$

$\phi_{2,10} = 0.2429462$

$\phi_{2,23} = 0.0$

$\phi_{2,24} = -8.124529 \times 10^{-3}$

$\phi_{1,29} = -8.715468 \times 10^{-3}$

Second flexible-body mode: i = 3

$\xi_3 = 0.005$ $\lambda_3 = 243.3$

$B_3 = 2.433$ $K_3 = 59198$

$\phi_{3,10} = -5.874251 \times 10^{-2}$

$\phi_{3,23} = 0.0$

$\phi_{3,24} = -2.388733 \times 10^{-2}$

$\phi_{3,29} = -4.071004 \times 10^{-2}$

TABLE II (cont)

NUMBERICAL VALUES USED IN THE ASPS STRUCTURAL MODEL
(Obtained from NASTRAN)

AVS Armature/Payload:

First rigid-body mode (z): i = 1

$\xi_1 = 0.0$ $\lambda_1 = 0.0$

$B_1 = 0.0$ $K_1 = 0.0$

$\phi_{1,1} = 0.0$

$\phi_{1,3} = -0.277196$

$\phi_{1,5} = 0.0$

Second rigid-body mode
(X and θ): i = 2

$\xi_2 = 0.0$ $\lambda_2 = 0.0$

$B_2 = 0.0$ $K_2 = 0.0$

$\phi_{2,1} = -0.3030391$

$\phi_{2,3} = 0.0$

$\phi_{2,5} = 6.554324 \times 10^{-3}$

Third rigid-body mode
(X and θ): i = 3

$\xi_3 = 0.0$ $\lambda_3 = 0.0$

$B_3 = 0.0$ $K_3 = 0.0$

$\phi_{3,1} = -0.3203905$

$\phi_{3,3} = 0.0$

$\phi_{3,5} = 8.807127 \times 10^{-4}$

TABLE II (cont)

NUMBERICAL VALUES USED IN THE ASPS STRUCTURAL MODEL
(Obtained from NASTRAN)

First flexible-body mode: i = 4	
$\xi_4 = 0.0$	$\lambda_4 = 564.5$
$B_4 = 5.65$	$K_4 = 318655$
$\phi_{4,1} = 0.6053111$	
$\phi_{4,3} = 0$	
$\phi_{4,5} = -2.02517 \times 10^{-2}$	
Second flexible-body mode: i = 5	
$\xi_5 = 0.005$	$\lambda_5 = 2739.4$
$B_5 = 27.4$	$K_5 = 7504413$
$\phi_{5,1} = -0.258577$	
$\phi_{5,3} = 0.0$	
$\phi_{5,5} = -5.618044 \times 10^{-2}$	

CONTROL LAW AND SIMULATION DEVELOPMENT

In the previous section, the flexibility models of the AGS and the ASPS were developed and a qualitative description of the operation of each was given. In this section, the control laws for each model will be developed and verified, as will be a quantitative expression for the time delay associated with the digital implementation of these controllers. Once all of the system blocks associated with each model have been defined, a General Stability Analysis (GSA) program file will be generated for each and will be used to predict system performance in the presence of unwanted disturbance inputs.

Design of AGS Control Law

The first step in the design of the AGS control law is to determine the plant characteristics as a function of frequency. This is done by using the structural data given in Table I and the form of the plant as shown in Figure 6. A plot of this uncompensated plant transfer frunction is shown in Figure 9. As the figure shows, two prominent flexible modes are superimposed on top of the rigid-body response. In order to provide good disturbance rejection, a bandwidth of approximately 1.0 Hz is desired. However, this will cause the peaking of the two bending modes to exceed 0 decibel, possibly resulting in instability. Several methods could be used to compensate such a response, the simplest of which would be pole-zero cancellation to eliminate the flelxibility effects. However, this method would run the risk of creating a system instability, due to the location of such poles. On a root-locus plot, these roots would appear as highly underdamped poles which are located very close to the imaginary axis. The intent of pole-zero cancellation would be to place a zero exactly on top of the pole, thereby removing this particular response from the overall system response. However, since the damping associated with modal roots can only be estimated and the modal frequency is not precisely known, the pole location associated with the mode is uncertain to a degree. Thus, if it were desired to place a zero directly on top of such a pole, it is quite possible and most probable that you would "miss". The danger associated with this occurrence is that the locus shape, for certain ranges of system gains, could possibly be driven into the right half-plane, thus creating an instability. Pole-zero cancellation is therefore to be avoided due to its high sensitivity to knowledge of the plant dynamics.

Another commonly used method of compensating a flexible structure with prominent modes is to phase-stabilize the open-loop response. The basic advantage of such an approach is that it will force any modal peaking (if modal frequency values are fairly accurate) to occur in the right-half plane of the Nyquist plane, away from the -1 point, no matter what the actual values of modal damping happen to be. This procedure will yeild a more robust design, meaning that even if modal peaks were to rise above 0 decibel, the resulting ringing would be damped out due to the location of the modal peaks in the Nyquist plane.

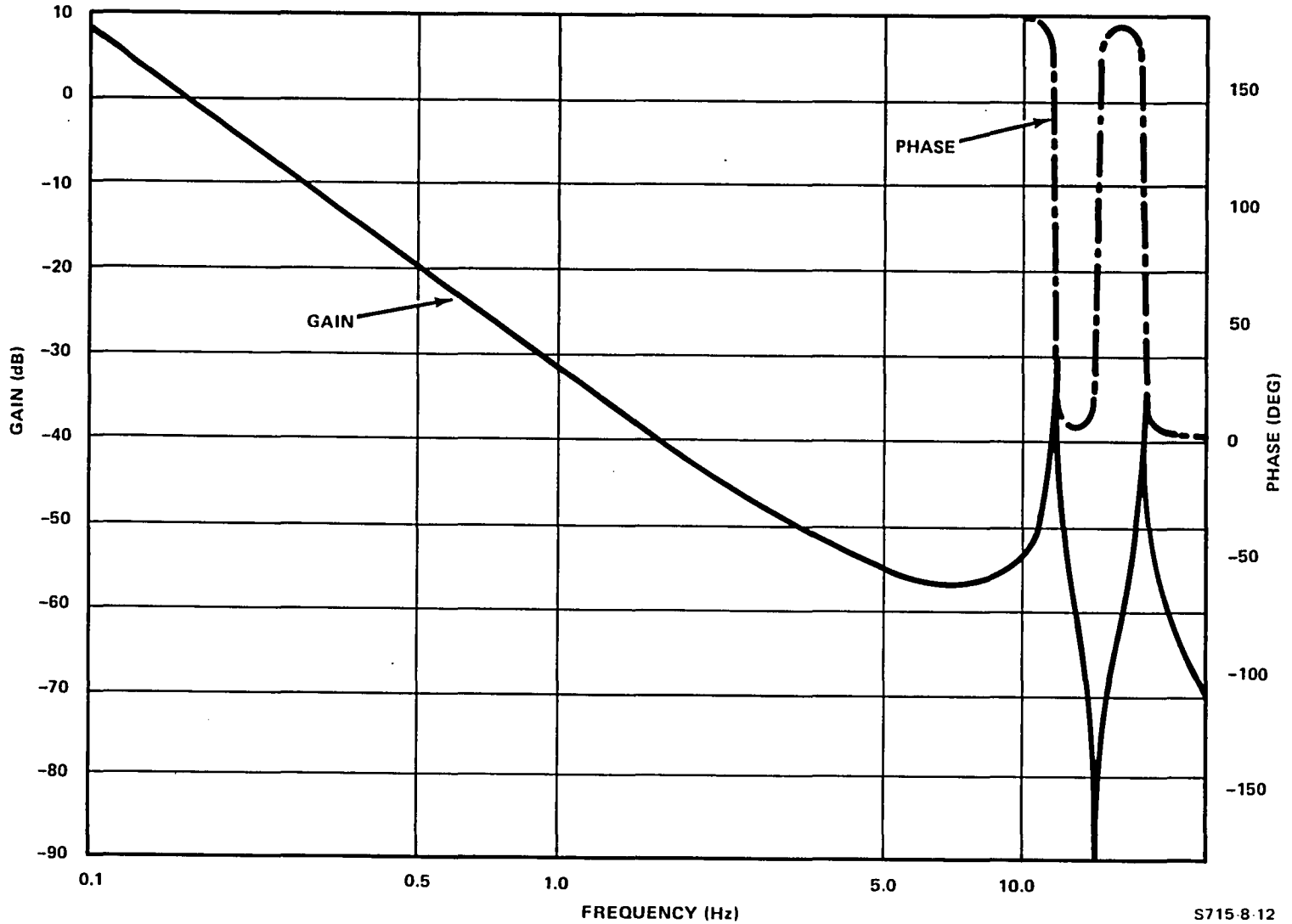

Figure 9
Uncompensated AGS Plant Transfer Function

The majority of the compensation design for the AGS control law was done on a Hewlett-Packard 5423 Structural Dynamics Analyzer, due to the speed and ease with which a design could be implemented, checked, and iterated to achieve the "best" open-loop margins and closed-loop performance. The analyzer designs were buffered with as much gain and phase margin as possible, so that when the complete AGS model (including the time-delay effects and IRU) was implemented on GSA, the resulting open-loop margins would be acceptable.

The initial step in the overall controller design was simply to use the plant shown in Figure 9 and, in an iterative fashion, to derive a P-I-D controller that would properly compensate the rigid-body portion of the transfer function. Once this task was completed, the resulting response was studied, and a bending mode filter (BMF) that would phase stabilize the flexible-body effects was developed. The two were "fine-tuned" in an iterative fashion and the final results are:

P-I-D Controller:

$$\text{P-I-D} = 117183\ [1.0098 + \frac{0.4488}{s} + 0.561s] \tag{15}$$

Bending Mode Filter:

$$\text{BMF} = \left(\frac{1 + 4s}{1 + 0.5s}\ \frac{1 + 0.0064s}{1 + 0.0266s}\right)\left(1 + \frac{2(0.5)s}{50.3} + \frac{s^2}{50.3^2}\right) \tag{16}$$

It can be seen from equation (16) that the bending mode filter is composed of a lead-lag network, a lag-lead network, and a complex pole pair. The purpose of the lead-lag is to add positive phase in the vicinity of the 0-decibel cross-over, while the lag-lead attenuates gain in the frequency band containing the modes. The complex pole pair gradually reverses the phase by 180 degrees (without adding peaking in the gain characteristic) such that the modes peak in the right half-plane of the Nyquist plane, away from the $-1 + j0$ point. The resulting open-loop plot, the corresponding Nyquist plot, and the closed-loop

response are shown in Figures 10 through 12, respectively. The open-loop characteristics of this response are:

crossover frequency (f_{CO}) = 0.56 hertz

gain margin = 20 decibels

phase margin = 60 degrees

while the closed-loop performance values are:

closed-loop bandwidth (f_{BW}) = 0.9 hertz

closed-loop peak = 1.0 decibel

highest modal peak = -4 decibels

The above system performance parameters were obtained under the assumption of an "ideal" system; i.e., no feedback dynamics and no digital affects. For completeness, these effects should be included and are now quantitatively defined.

The inertial reference unit (IRU) is used to provide feedback information for an inertial pointing system such as the AGS; its dynamic effects have been widely documented (ref 3) and are

$$\text{IRU} = \frac{1}{\left(1 + \frac{1.6s}{94} + \frac{s^2}{(94^2)}\right)\left(1 + \frac{1.2s}{324} + \frac{s^2}{(324^2)}\right)} \qquad (17)$$

At the previously-defined crossover frequency (f_{CO}), the additional phase lag caused by these dynamics is approximately 3.5 degrees, leaving a net phase margin of 56.5 degrees.

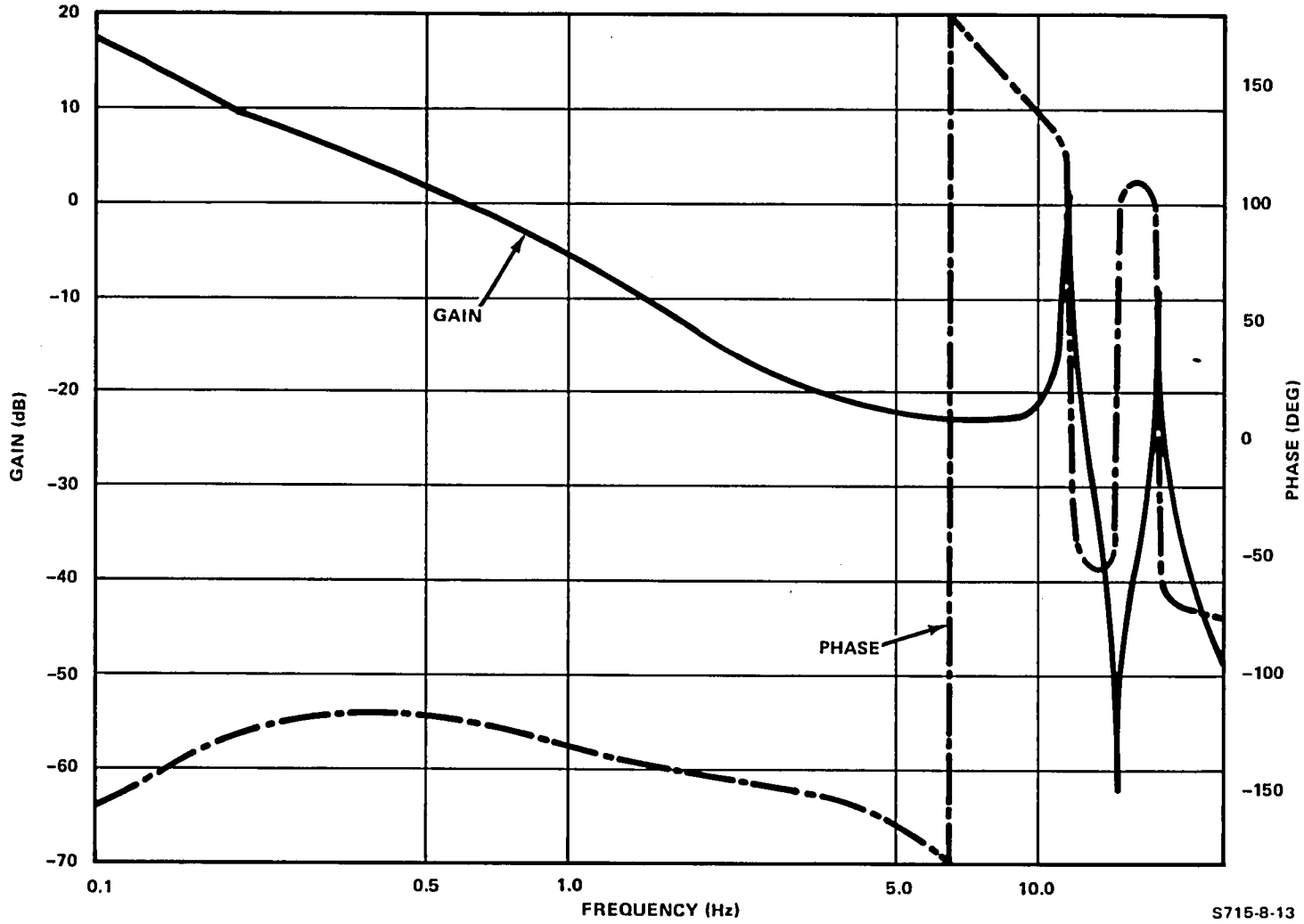

Figure 10
AGS Open-Loop Transfer Function

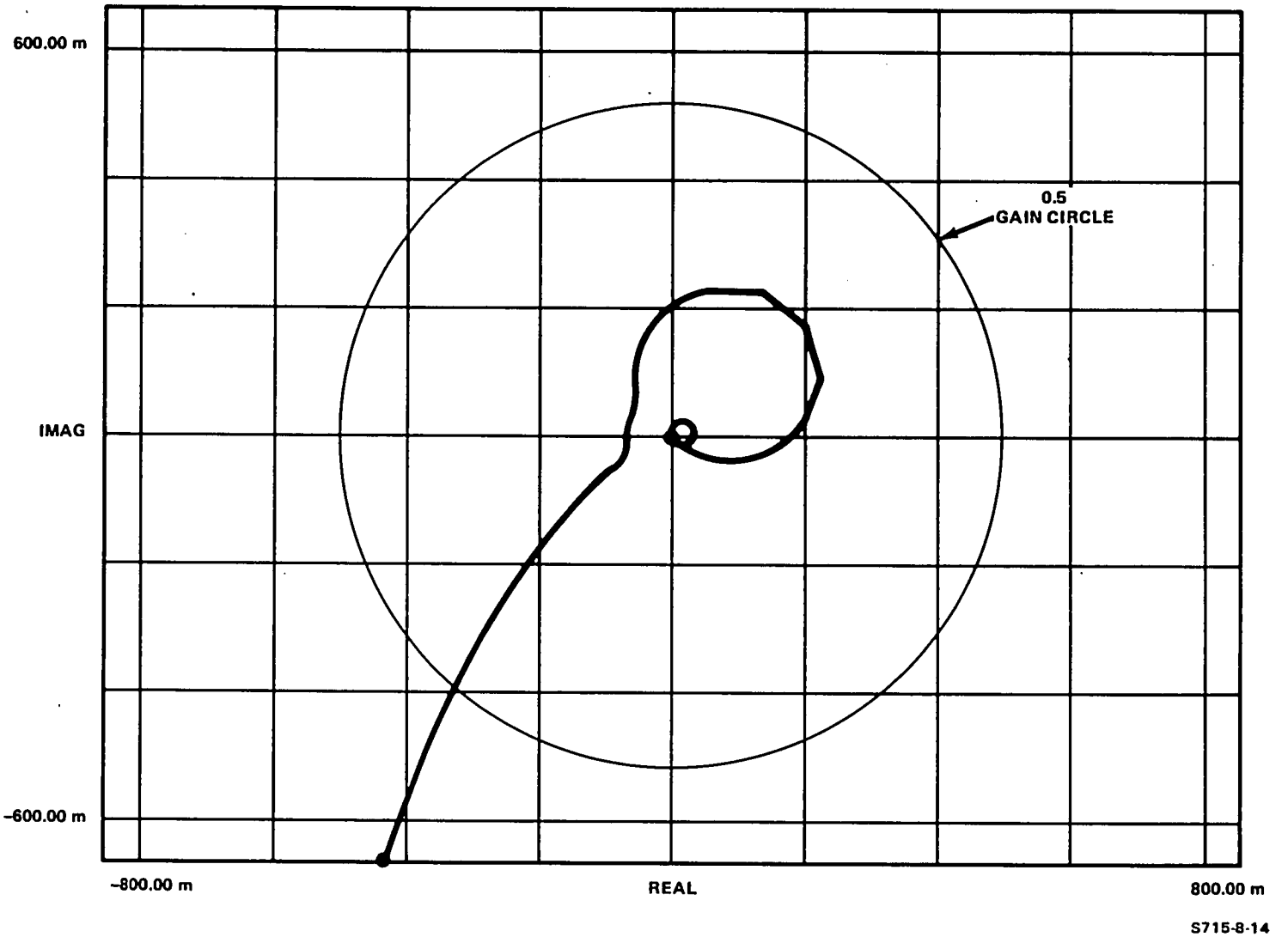

Figure 11
Nyquist Plot of AGS Open-Loop Transfer Function

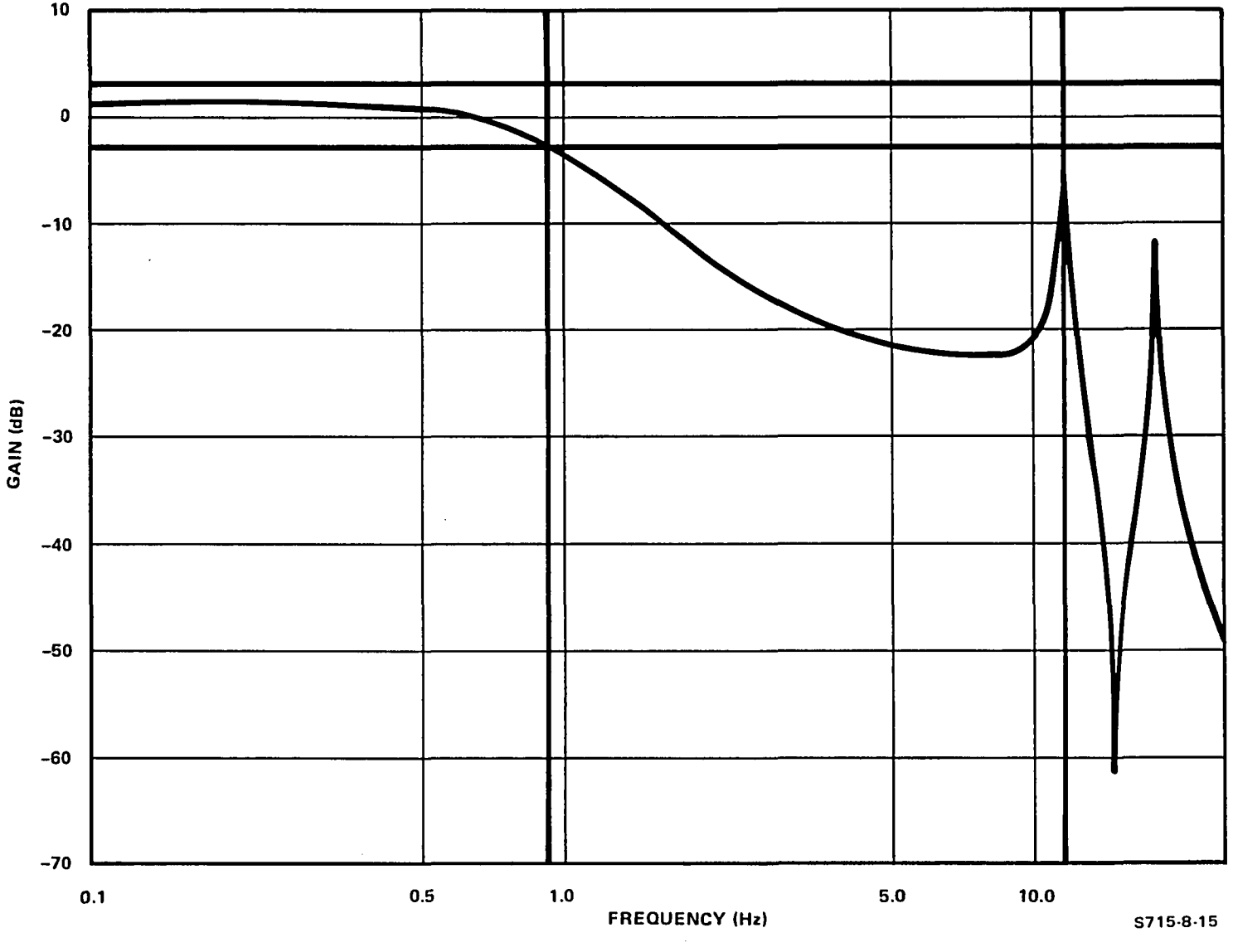

Figure 12
Phase-Stabilized AGS Closed-Loop Transfer Function

Digital effects can have significant impact on the phase margins of a control system and, hence, on the achievable bandwidth of the control loops. In this study, two sources of digital phase lag are considered; sample and hold, and transport delay. The sample-and-hold (S-H) effect actually involves a gain roll-off, as well as a phase lag. However, if the sample frequency is significantly higher than the control-loop bandwidth, then the S-H can be approximated as a pure phase lag of the form

$$e^{-j\pi\omega/\omega s}$$

where ωs is the sample frequency, assumed to be 100 hertz for both the AGS and ASPS configurations. Similarly the transport delay is modelled by a pure phase lag

$$e^{-j\tau_d\omega}$$

where τ_d is the transport delay time. As shown, the phase lag expression cannot be included in the linear AGS and ASPS models. However, a Pade approximation of the complex exponential, consisting of a polynomial quotient with approximate unity gain and linear phase characteristics, can be included in the models. A third-order approximation was determined to be adequate. A combined effective delay, $(\pi\omega/\omega s + \tau_d)$, of 0.01 second based on a τ_d of 0.05 second has been assumed.

It is recognized that a stability analysis of a sample data system performed by adding a time delay to the continuous plant will not give the same results achieved by performing a sample data stability analysis. However, in this study, the continuous system stability margins should be close to the sample data values, since the ratios of half-sample frequency to open-loop crossover frequencies are large.

The time-delay exponential takes the form

$$e^{-0.01s} = \frac{D(-s)}{D(s)} \qquad (18)$$

where D(s), for a third-order approximation, is

$$D(s) = 1 + 0.005s + 1.0714 \times 10^{-5}s^2 + 1.1905 \times 10^{-8}s^3 \qquad (19)$$

Substituting equation (18) into (19) and simplifying yields the expression

$$e^{-0.01s} = \frac{(377 - s)\ (s^2 - 530s + 222846)}{(377 + s)\ (s^2 + 530s + 222846)} \qquad (20)$$

This expression was synthesized on the analyzer and was found to have a unity gain, linear-phase dropoff relation at frequencies up to 25 hertz. However, the phase of a second-order approximation, obtained in a similar fashion, began to distort at the higher frequencies. Thus, since unity gain and linear phase dropoff is desired, the third-order approximation can be used in good faith and will yield good results over the frequency range of interest. At the previously stated crossover frequency, the additional phase lag created by the time delay is approximately 2 degrees, leaving a net phase margin of 54.5 degrees after the IRU and time delay have been considered.

Design of ASPS Control Laws

This subsection addresses the development of the control laws associated with the ASPS model. The approach taken is similar to that used on the AGS model; i.e., the preliminary designs are done on the analyzer as single-input/single-output loops. These designs are buffered with as much gain and phase margin as possible, for the same reasons given in the AGS design section. The three AVS loops are independently designed, and then included as the control law in the dynamic, cross-coupled AVS model to be implemented on GSA. The stability of each of the three AVS loops is then verified with the other AVS loops closed, and the "best" performance for each of these loops is obtained by successive iterations on GSA. Once the AVS loops have been adequately stabilized, the AGS follow-up mode controller is designed.

There are three main objectives in defining the various magnetic and gimbal control-loop bandwidths for the ASPS configuration. First of all, the disturbance rejection capability of the inertial pointing loop should be maximized by defining as large a pointing-loop bandwidth as possible. Secondly, the level of disturbance seen by the pointing loop should be minimized by minimizing the translations and follow-up loop bandwidths. Finally, the first two objectives must be satisfied while maintaining adequate stability margins and reasonable magnetic actuator gaps. In general, the stability margin requirement imposes an upper limit on all of the loop bandwidths, while the gap requirement defines a lower bound to the follow-up and translation-loop bandwidths. Because of the gap requirement, it is considered desirable to close the follow-up and translation loops at roughly the same bandwidths that have been used in past ASPS studies. Thus, a 0.2-hertz translation-loop bandwidth and a 0.5-hertz gimbal-loop bandwidth were established as goals for the compensator designs.

The first step in the design of the AVS translational loops is to identify the strutural plant that each compensator controls. This task was done with the aid of Figure 8 and the data in Table II. These transfer functions were synthesized on the analyzer and shown to be essentially rigid-body responses over the frequency range of interest (highest modal peak is -70 decibels and occurs at 89.9 hertz). Thus, the design of a P-I plus lead-lag controller to stabilize such a response is a relatively straightforward procedure. The P-I plus lead-lag compensation was chosen because it is the simplest compensator form that zeros a bias error while stabilizing a $1/S^2$ plant and producing a S^{-2} high frequency rolloff.

These controllers are, after rearranging the classical expression, of the form

$$G_X(s) = G_Z(s) = K_P K_I \frac{(1 + s/K_I)\,(1 + s/\omega_1)}{S\,(1 + s/\omega_2)} \qquad (21)$$

Equation (21) is used in conjunction with the rigid-body response of $1/Ms^2$ to obtain the desired open-loop transfer function. This open-loop response was synthesized on the analyzer and, after itertation, a controller that yielded good open-loop margins and closed-loop response characteristics was found and is

$$G_X(s) = G_Z(s) = 0.04113 \frac{(1 + 15.92s)\ (1 + 15.92s)}{s\ (1 + 0.592s)} \qquad (22)$$

This controller in cascade with the rigid-body plant ($1/13.016s^2$) yields the following open-loop values:

Crossover frequency (f_{CO}) = 0.12 hertz

Gain margin = ∞

Phase margin = 56.5 degrees

The corresponding closed loop characteristics are:

Closed-loop bandwidth (f_{BW}) = 0.19 hertz

Closed-loop peaking = 1.35 decibels

At the crossover frequency, the additional phase lag caused by the system time delay is calculated from equation (20) and is approximately 0.4 degree.

The AVS pointing loop controller is designed in basically the same manner as were the translational controllers; however, due to the non-unity feedback (IRU is used in AVS pointing loop) and the presence of modal peaking in the open-loop response, care has to be taken to ensure that such peaking does not occur in the closed-loop response. The reason for this can be seen if one envisions the form of a generic closed-loop control system. In other words, if R is the system input, C is the output, G is the forward path transfer function, H is the feedback path transfer function, and E is the error signal, then the following statements can be made:

a. The stability of the open-loop transfer function is found by studying the frequency response of the product GH. From an input/output relationship, the stability is determined by the gain-phase

characteristic of the product GH operating on the error E. The cumulative product is then compared to the input R at the summing junction.

b. The output response C is equal to the open-loop transfer function G operating on the same error signal E.

It can be seen from statements a and b that, if G has modal peaking in its frequency-response characteristic and H is sufficiently low pass in nature (in the frequency range containing this peaking), then it is possible that the peaking would not affect system stability at all, but would show up in the closed-loop response as lightly damped "spikes". It should be emphasized that these spikes do not create a system instability, but would cause ringing in the time response if they were not attenuated. Such a situation was encountered when stabilizing the AVS pointing loop. A P-I-D controller was used to stabilize the pointing loop, and no problems were anticipated due to the shape of the open-loop plant transfer function. A P-I-D design was used that yielded a 16-decibel gain margin of 50 degrees of phase margin; yet when the loop was closed, a stable modal peak of 24 decibels occurred at 89.9 hertz (first payload mode). To reduce this closed-loop peaking, a bending mode filter was added as part of the pointing loop controller. The frequency response dictated that the bending mode filter should have a lightly damped zero at 700 radians per second and a heavily damped (Q=1) pole at 100 radians per second. In equation form this bending mode filter is

$$BMF = \frac{1 + (0.1/700)s + s^2/700^2}{1 + (1/100)s + s^2/100^2} \tag{23}$$

This filter was added to the GSA simulation, and a P-I-D controller was then designed that would compensate this "new" plant. After several iterations, one was determined that gave good open-loop margins as well as closed-loop performance. Its equation is

$$P\text{-}I\text{-}D = 22865\ (21 + 18/s + 8.8s) \tag{24}$$

The controller, in conjunction with the bending mode filter in equation (23), gives the following system performance:

Open loop:	crossover frequency (f_{CO}) = 1.4 hertz
	gain margin = 13 decibels
	phase margin = 54 degrees
Closed loop:	bandwidth (f_{BW}) = 2.8 hertz
	peak = 2.3 decibels
	highest modal peak is -16 decibels at 89.9 hertz

As can be seen from these results, the bending mode filter did successfully attenuate the modal peaking without any detrimental effects on pointing performance stability.

As a last check to verify these loops, each loop in the AVS portion of the GSA model was opened in succession while the other two loops were left closed. The input of the open loop was then excited, and its open-loop transfer function was determined and checked for stability. Each of the three loops showed more than adequate open-loop margins (at least 10 decibels gain margin and 40 degrees phase margin). Thus, it is assured that the AVS model is stable and will operate properly.

The last step in the completion of the ASPS model is to determine the controller for the elevation gimbal axis, as the AGS operates in the follow-up mode. In this particular mode, the input to the AGS control law is the payload tilt angle (obtained from a gap transformation matrix), while the feedback signal is the inertial angle on the AGS side of the magnetic interface. The purpose of this mode is to keep the AGS aligned with and following the motion of the payload body as it moves in the gap, such as during a tracking maneuver. The nature of this particular operation dictates that the elevation gimbal follow-up mode controller "sees" the entire system dynamics - the AGS, AVS, and the uncancelled reaction forces and torques exerted by the AVS on the AGS. Keeping these facts in mind, the complete open-loop transfer function, from the

follow-up mode input to the AGS inertial angle output, was run on GSA and was found to be a rigid-body response of $1/1146s^2$ out to at least 10 hertz. Since it was desired to close this loop at a bandwidth of approximately 0.5 hertz, no problems were anticipated.

The type controller to be used for this mode is a P-I plus lead/lag of the same generic form as that given by equation (21). The design was done on the analyzer and the resulting controller is

$$G_{FUM}(s) = 254 \frac{(1 + 6.37s)\ (1 + 1.54s)}{s\ (1 + 0.172s)} \tag{25}$$

When using this controller, the open-loop characteristics for the follow-up mode are:

crossover frequency (f_{CO}) = 0.34 hertz

gain margin = ∞

phase margin = 49 degrees

The corresponding closed loop response is:

bandwidth (f_{BW}) = 0.58 hertz

closed-loop peaking = 2.9 decibels

Such a closed-loop response should be more than adequate for this particular AGS application.

AGS PERFORMANCE EVALUATION

System performance for both the AGS and ASPS configurations is defined by the inertial pointing stability achieved in the presence of shuttle disturbances (as defined in the above section on model development). Using the GSA models developed for the study, performance stability is experssed most conveniently by the frequency transformation from disturbance input to inertial payload angular motion. On option, a time history of the system response to a step disturbance input can be generated.

In this section, the block diagram shown in Figures 6a and 6b were used to obtain a frequency response of the transfer function, relating an AGS base force disturbance input to the payload pointing angle output. This was done by setting the GSA variable R(32) (shown in Figure 6b) to unity and monitoring the output angle θ_o. A Bode plot of this response is given as Figure 13. As this figure shows, the low-frequency asymptote has a +3 slope and there is no high-frequency rolloff. The theory which supports these findings has been described in detail in reference 5 and so will be covered only briefly in this report. The low-frequency asymptote of slope +3 is due to the -3 slope in the open-loop response characteristic. The lack of a high-frequency rolloff is caused by the fact that an end-mount pointing system such as the AGS provides a rigid-link path for translational motion between its base and the supported payload. For this reason, high-frequency vibration can and will transmit directly to the payload, and the elevation gimbal controller can do little in the way of rejecting such a disturbance at frequencies above its bandwidth. The value of the peaking at the high frequency will be greater if the mass/inertia ratio of the portion of the system above the controlled axis is increased and will be less if this ratio is decreased. The peak value of the response occurs at the first AGS flexible mode, while the smaller peak is possibly due to the 20-hertz payload.

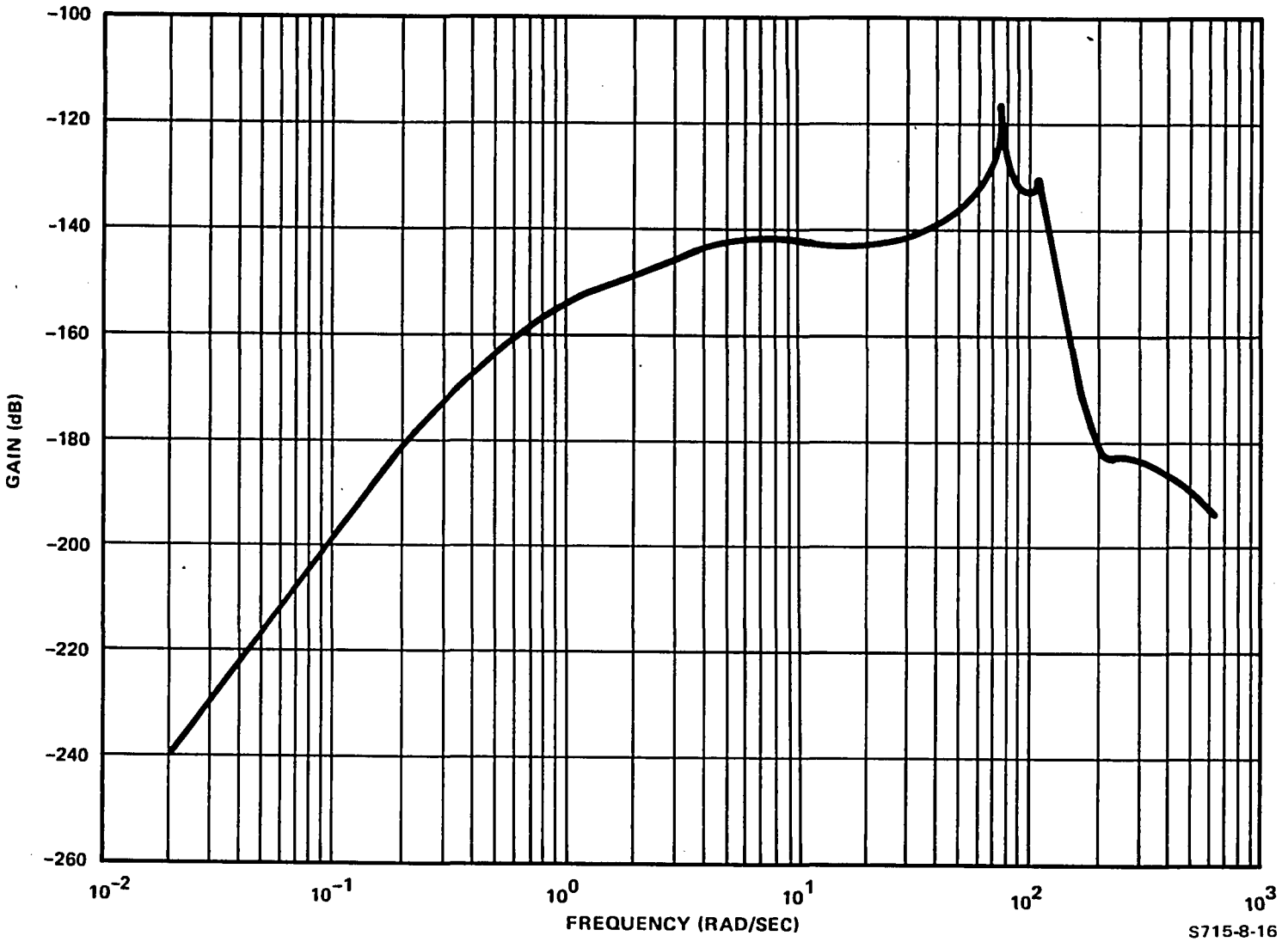

Figure 13
AGS Pointing Error for Unity Base Input

The AGS time response was done on GSA in basically the same manner as was the frequency response; however, the system input for this portion of the study is a VRCS torque pulse applied about the shuttle Z_0 (yaw) axis. In Figure 5, the magnitude of this pulse is given as 22937 inch-pounds. This input is applied by setting R(31) of Figure 6b in the simulation to this value. The GSA program, for the time-response option, interprets this input as being a step occurring at time zero. This input is assumed to last for 0.24 second. The system angular time response then will decay to zero in the manner dictated by its dynamic characteristics. This particular response was obtained from GSA in a piecewise linear fashion by exciting R(31) with the VRCS torque value mentioned above and running a 0.24-second time response for every system variable. For the next portion of the run, this input was removed, and each dynamic state input and output was initialized with its position and velocity (initialized as required by the corresponding differential equations) at 0.24 second. The model was then run again with these initial conditions being the system drivers, and the output angle was monitored for 5 seconds. The resulting response is shown in Figure 14. The peak pointing error due to the VRCS disturbance input is 7.4 arc seconds, while the negative swing peaks at 1.5 arc seconds. It can also be seen that the response begins to decay toward zero error at 5 seconds and that modal peaks (which could have caused system ringing) have been adequately and successfully attenuated.

ASPS PERFORMANCE EVALUATION

The model shown in Figures 8a and 8b was used in this section to perform a detailed analysis of the effects of payload structural flexibility and misknowledge of the payload's effective CM location on the pointing performance of the ASPS. A parametric study of the predicted CM location (implemented as part of the control law) versus the actual CM location, with and without the effects of payload flexibility, was done; and the results are included and discussed in this section.

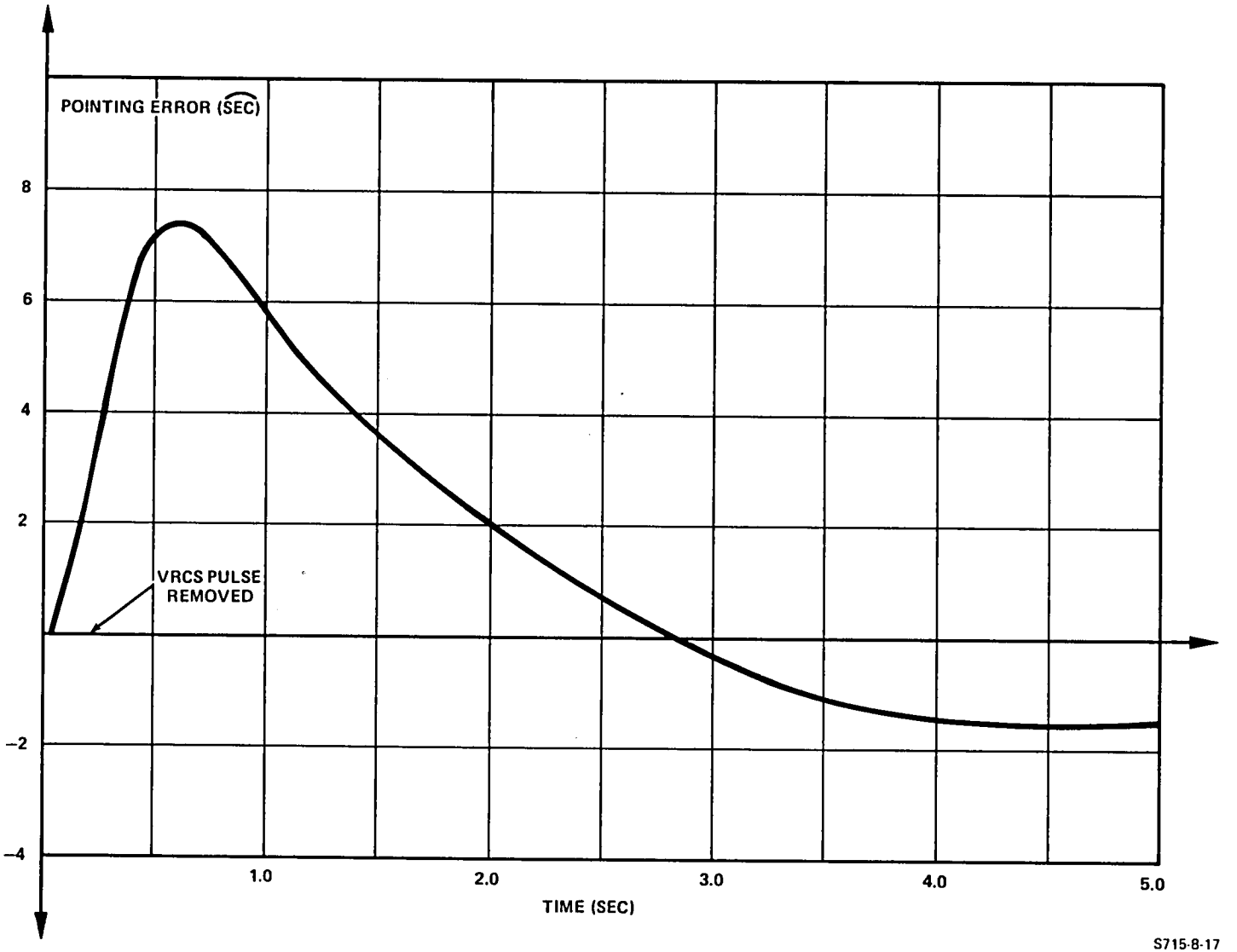

Figure 14
AGS Time Response to 0.24 Second, Shuttle VRCS Yaw Maneuver

The first step taken in this study was to determine the actual location of the payload CM. Figure 7 shows that the distance between the magnetic actuator plane and the payload CG is 59.1 inches. In the NASTRAN formulation, however, 11.4 mass units are placed at node 10P and 1.6 mass units at node 9P. This procedure yields an "effective" CM location of [11.4/(11.4+1.6)](59.1"), or 51.83 inches above the actuator plane. Thus, if it were desired to decouple translational and rotational motion completely, the value of the moment arm ℓ_1 shown in Figure 8b would be set to 51.83 in the appropriate control law. However, it would be unrealistic to assume that one could precisely locate the effective CM of a payload; thus a worst case ±1 percent uncertainty (both high and low extremes) is used in the study. As an example of this decoupling law error, consider the case of 99 percent payload CM knowledge. This terminology means that, since the actual effective CM location is 51.83 inches, but the value of ℓ_1 used in the decoupling law is only 51.31 inches, perfect decoupling is not achieved. In the case of 101 percent knowledge, the value of ℓ_1 to be used in the decoupling law is 52.35 inches, again meaning that perfect decoupling would not occur.

The response studied in this section is, as in the AGS case, the transfer function relating an AGS base unity input to the payload pointing angle. However, in the ASPS phase of the study, this response was done as a payload CM offset study with both a rigid and a flexible payload. From a simulation standpoint, the Bode plots were obtained by setting the GSA variable R(33) (shown in Figure 8a) to unity and monitoring the output angle $\theta_{\gamma 9p}$. Payload flexibility was removed by inserting a logic switch in series with each flexible payload mode and setting the values to zero. The units of each plot are radians per pound, expressed in decibels. Thus, if it were desired to convert to arc seconds per pound (in decibels), an addition of 106.3 decibels would have to be made to each point on the curve.

The results of thd CM offset-payload flexibility study are shown in Figures 15 through 20. As the figures show, these responses have the same low-frequency asymptote (+3 slope) as does the AGS response; however, as a worst case, the ASPS response is approximately 60 decibels down when compared to the AGS case. This greater low-frequency attenuation is due to the fact that the AVS pointing loop could be closed at a higher bandwidth than could the AGS pointing loop. This illustrates one advantage of magnetic suspension when considering system flexibility effects. Structural flexibility was the major system aspect that determined the AGS pointing-loop bandwidth, whereas it is not a factor when stabilizing the AVS loops. This is due to the physical separation of the AGS and the payload at the magnetic interface. The modal frequencies associated with each body are now sufficiently high that they do not affect system stability in the range of bandwidths associated with the AVS loops.

Another major advantage of magnetic suspension is the presence of a high-frequency rolloff that the AGS response does not have. This rolloff is caused by the slope of the high-frequency portion of the AVS translational-loop/open-loop transfer function [ref 5] and could be even more pronounced if a higher order controller/filter were to be used. This rolloff illustrates the concept of isolation; at high frequency, it is possible for the payload to remain essentially motionless and allow the base to move around it. Thus, from the standpoint of isolation capability, a very low translational bandwidth would be desirable. However, the lower limit on this bandwidth is usually dictated by the maximum available gap in the MBAs. Since this gap size determines to a great extent the system power and weight requirements, the "optimal" setting of the translational-loop bandwidth would involve a tradeoff study of the amount of isolation capability desired versus the power and weight requirements needed to ensure proper system operation under these conditions.

The effects of payload flexibility are also evident from the high-frequency characteristics of Figures 9 through 15. With payload flexibility included in the model and simulation, the translational controllers sense the motion caused by payload flexibility effects and interpret it as being rigid-body motion. The resulting controller action creates a high-frequency rolloff that is not as

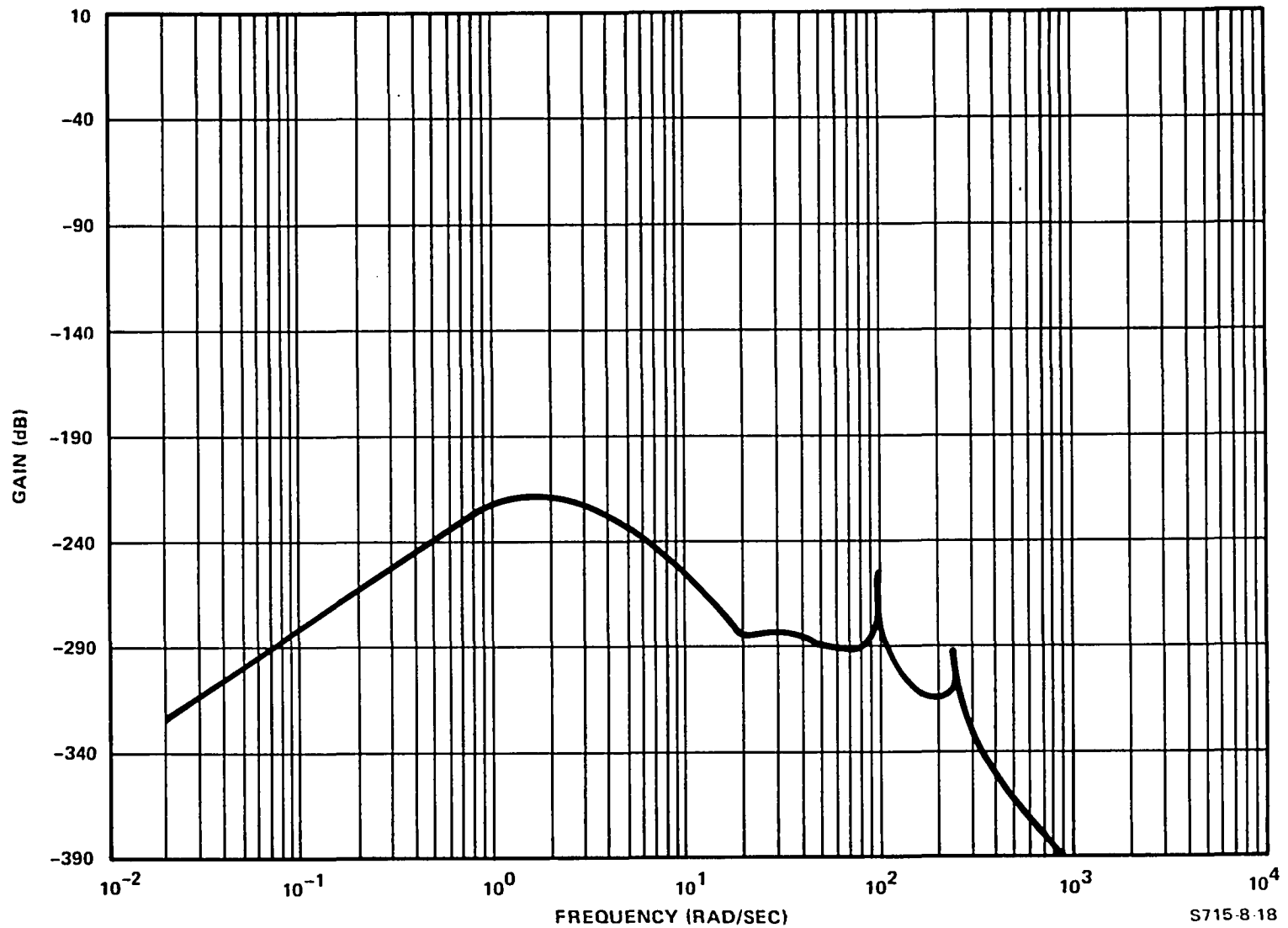

Figure 15
ASPS Frequency Response for AGS Base Input
No Error in CM Offset Estimate, No Payload Flexibility

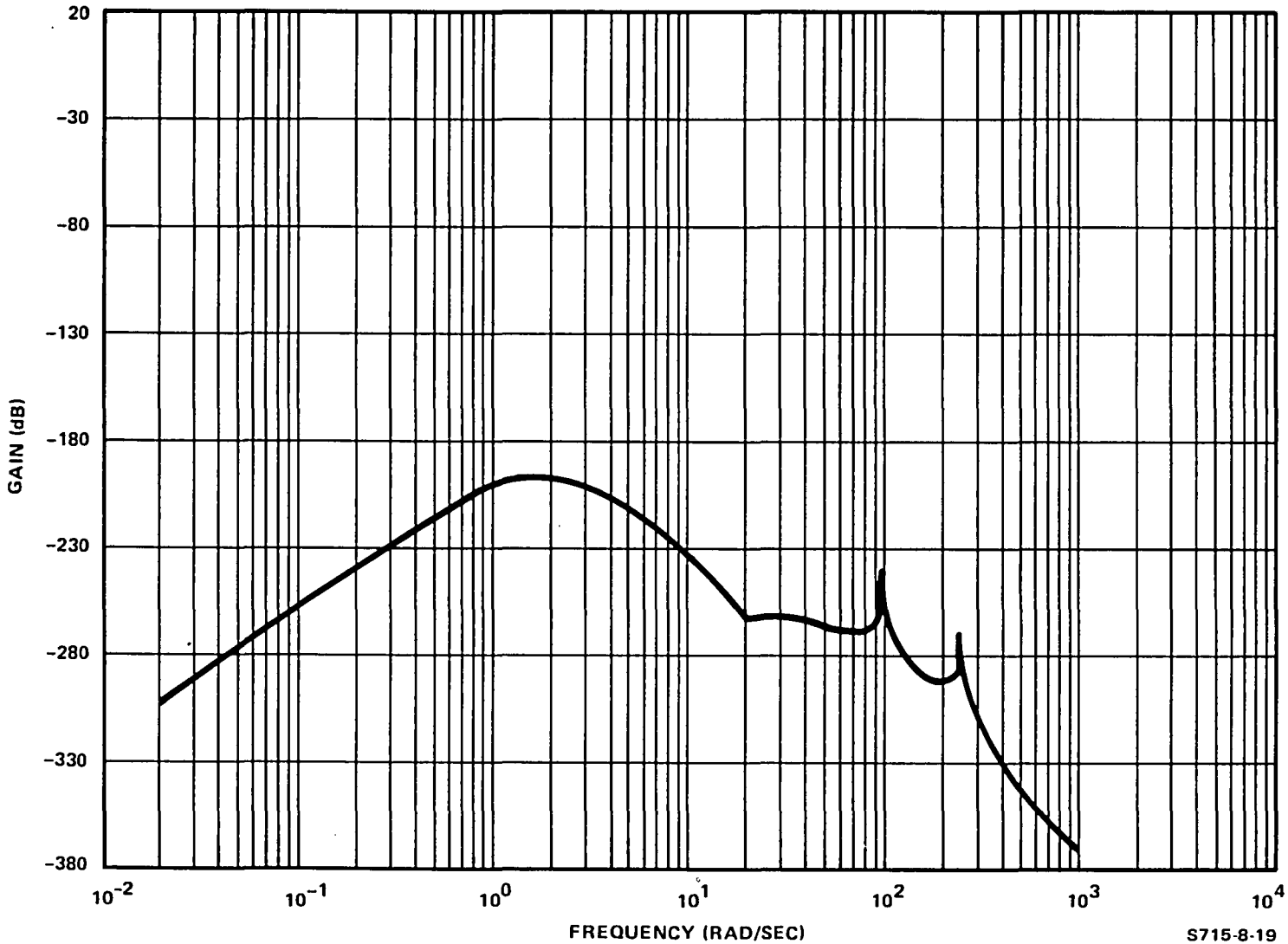

Figure 16
ASPS Frequency Response for AGS Base Input
-1 Percent Error in CM Offset Estimate, No Payload Flexibility

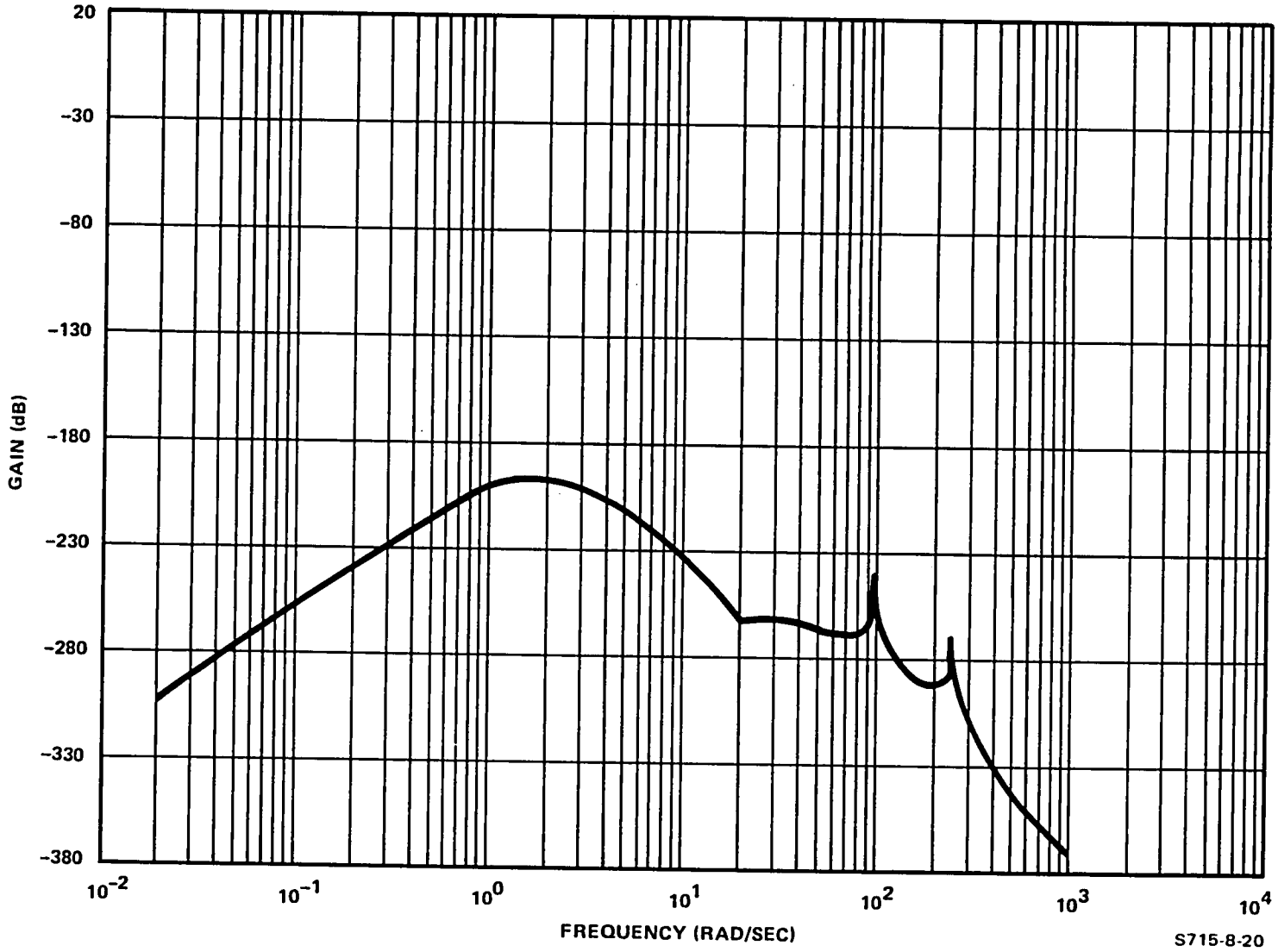

Figure 17
ASPS Frequency Response for AGS Base Input
+1 Percent Error in CM Offset Estimate, No Payload Flexibility

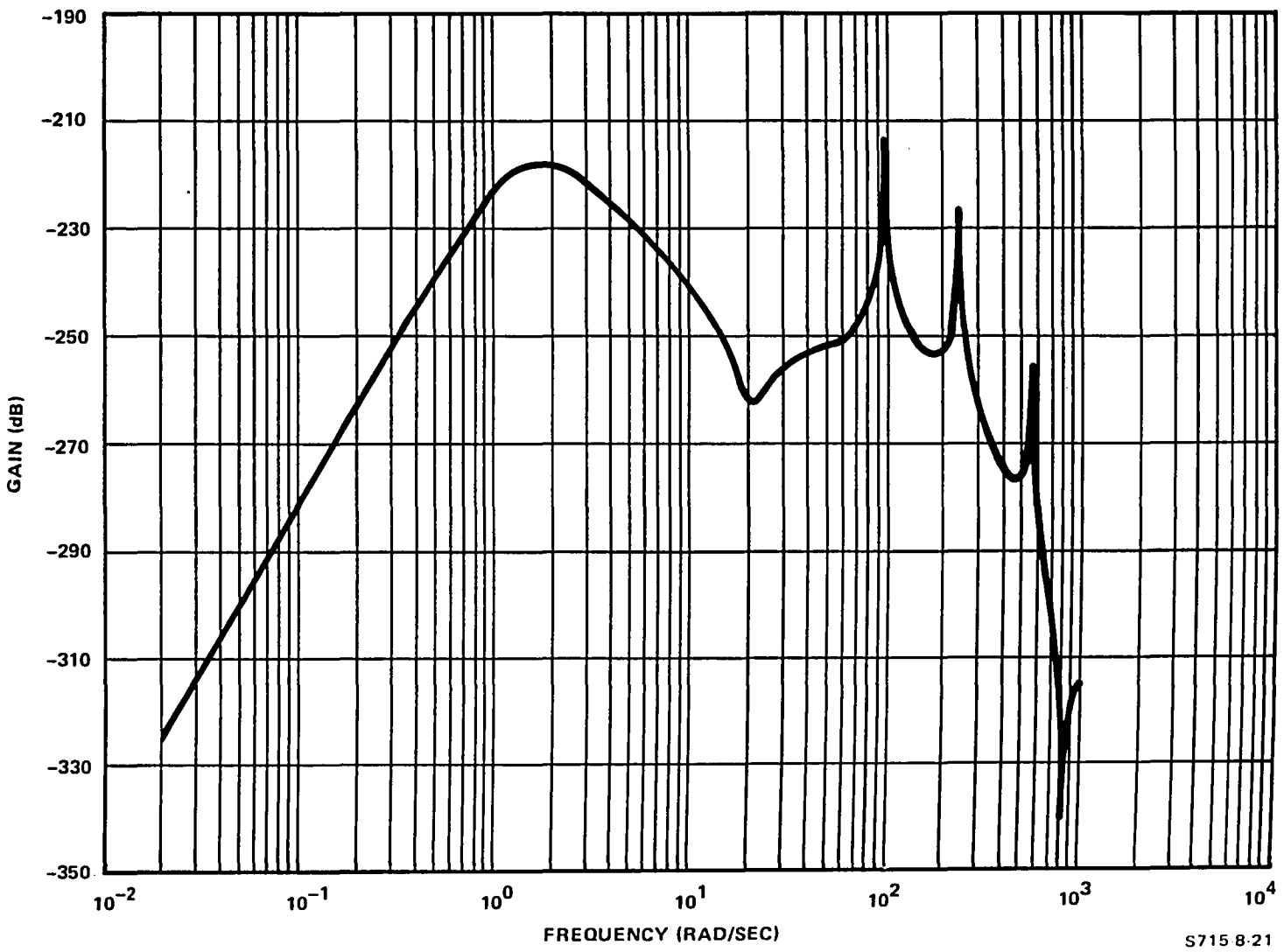

Figure 18
ASPS Frequency Response for AGS Base Input
No Error in CM Offset Estimate, No Payload Flexibility

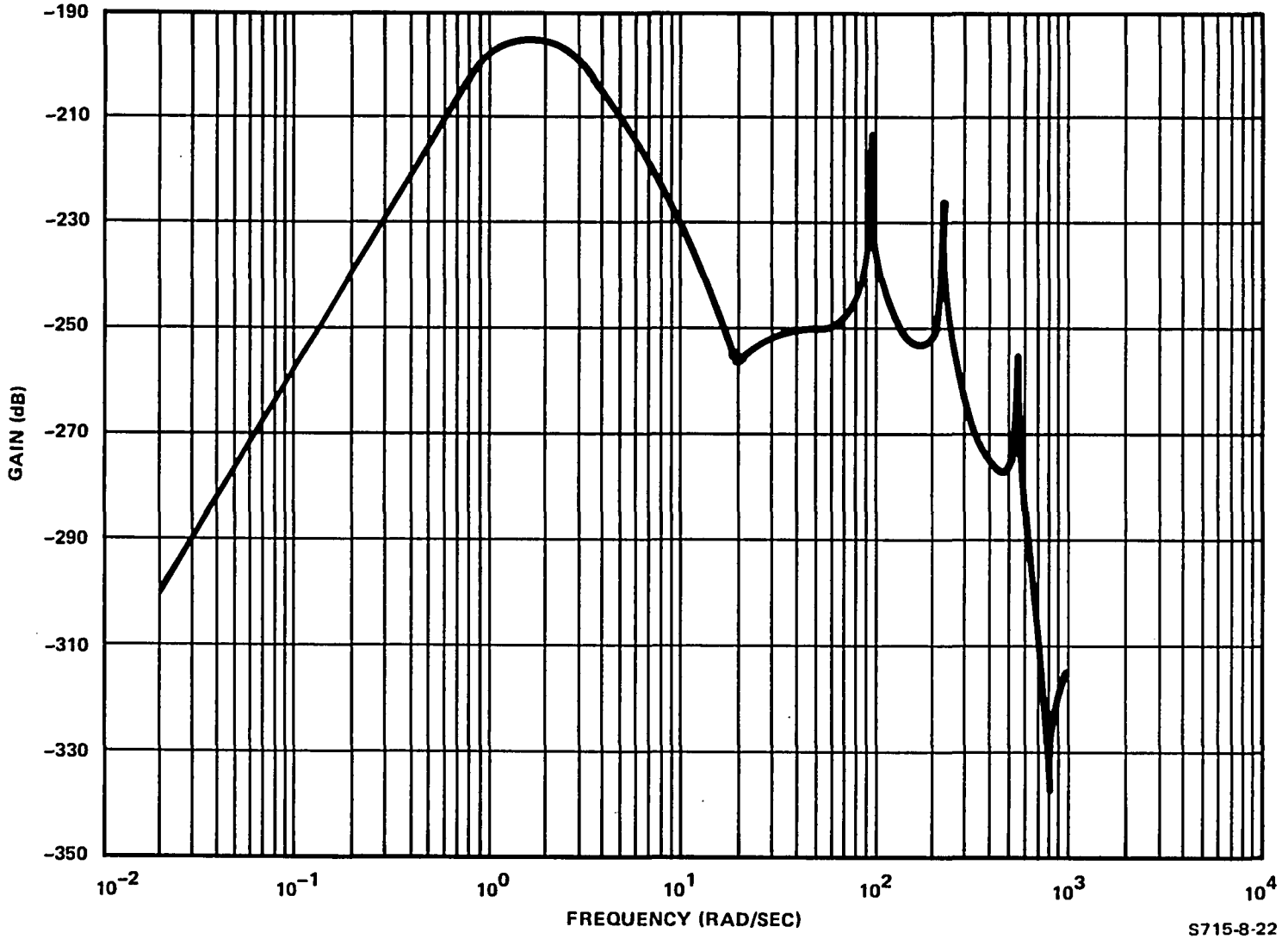

Figure 19
ASPS Frequency Response for AGS Base Input
-1 Percent Error in CM Offset Estimate, No Payload Flexibility Included

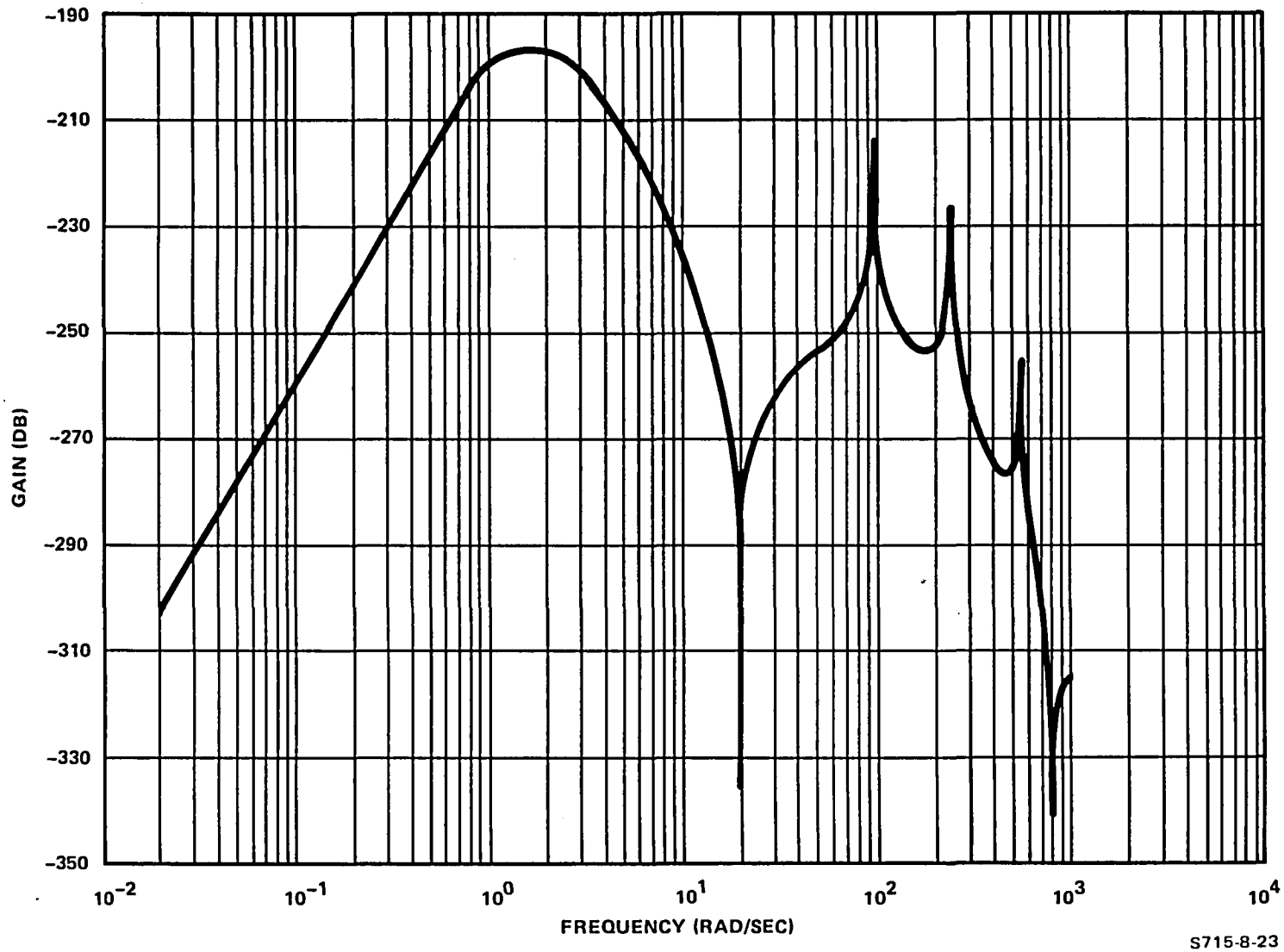

Figure 20
ASPS Frequency Response for AGS Base Input
+1 Percent Error in CM Offset Estimate, Payload Flexibility Included

pronounced as those obtained from the rigid-body payload simulation. The results of the payload CM offset/flexibility study are summarized in Table III.

TABLE III
RESULTS OF ASPS CM OFFSET STUDY

	LF Gain (dB) (0.01 RPS)	Isolator Peak Value (dB)	HF Gain (dB) (1000 RPS)
No Payload Flexibility:			
100% CM Knowledge	-343	-219	<-400
99% CM Knowledge	-319	-195	-373
101% CM Knowledge	-320	-196	-374
Payload Flexibility Included:			
100% CM Knowledge	-343	-218	-315
99% CM Knowledge	-319	-195	-315
101% CM Knowledge	-320	-196	-315

Another interesting point to be made concerning Figures 9 through 15 is the occurrence of zeros whose damping coefficients vary over a wide range of values. This fact is most likely caused by the parallel structure that exists between a given AVS controller output command and the payload pointing angle. In other words, one could represent such a parallel structure as a single input/single output transfer function block through the use of simple algebraic manipulations. By studying the ASPS NASTRAN data given in Table II, noting both magnitude as well as sign, it should be evident that odd-looking zeros would appear.

An attempt was made at obtaining a time response for the ASPS model, but, unfortunately, numerous problems occurred with the time-response option available on GSA which could not be resolved in a timely manner.

However, even though the ASPS time response was not obtained, a fairly accurate estimate of its maximum value can be made by using the results presented in this report. By comparing the data shown in Figures 9 and 14, it can be seen that the low-frequency response of the AGS and ASPS have the same general shape up to approximately two RPS. Reference 5 has shown that this portion of such responses is due to the pointing-loop dynamics. Thus, if it can be shown that the majority of the energy contained in the AGS base force input caused by Shuttle motion is at frequencies below 2 RPS, then the peak value of the ASPS time response can be determined by simply multiplying the AGS peak response (7.4 arc seconds) by the direct magnitude ratio of the 2 frequency responses below 2 RPS. Such an analysis was performed and discussion of the procedure and results follow.

The first step in the procedure is to determine the Fourier transform of the 0.24-second VRCS torque pulse shown in Figure 6. The resulting expression is given as

$$F(j\omega) = 5505 \frac{\sin (0.12\omega)}{0.12\omega} \tag{25}$$

This Shuttle torque disturbance input is then applied to the AGS base as a force through the Shuttle-pallet dynamics as shown in Figure 8a; thus, it is desired to show that most of the energy contained in the resulting frequency domain transfer function is at frequencies below 2 RPS. Such a procedure was programmed, and the results clearly indicated that essentially all energy was below 0.1 RPS. As an example, the following three points denoted by ω (gain in dB), illustrate the concept: (0.01,148), (0.1,108), and (2.0,58). Note that the difference in gain from 0.01 RPS to 2.0 RPS is a decrease of over four orders of magnitude. Therefore, the direct ratio method for determining the ASPS peak error can be used with a high degree of confidence.

The data given in Figures 9 and 15 show that there is a low-frequency gain attenuation associated with the ASPS response of 60 decibels (factor of 0.001). Thus, the peak pointing error associated with the ASPS disturbance response is (0.001) x (7.4 arc seconds), or 0.007 arc seconds. Such an estimate is "in the ballpark," so to speak, of values obtained in previous study phases associated with the ASPS program. Lastly, due to the fact that the ASPS pointing loop is closed at a higher bandwidth than is that of the AGS, it can also be stated that the time response characteristics associated with the ASPS disturbance response will be much faster than that of the AGS (see Figure 9).

CONCLUDING REMARKS

In this report, the impact of structural flexibility on the pointing performance of the AGS and the ASPS has been assessed. It was found that the AGS required a phase-stabilized design to eliminate the possibility of modal peaking affecting system stability. In addition, the bending mode filter implementation for wide-angle operation of the AGS will require the use of a tracking algorithm to compensate for the modal variances over the entire range of system attitudes. In the ASPS case, the threat of system instability due to modal peaking was never an issue; however, a bending mode filter was required to attenuate a stable modal peak in the AVS pointing-loop/closed-loop response. Due to the small angle motion of the AVS, a tracking algorithm would not be needed with this filter, however.

The frequency response characteristics of the AGS and ASPS disturbance responses do indeed assume the theoretical shapes of an end-mount pointing system and an end-mount pointing and isolation system, respectively. The AGS response does not have a high-frequency rolloff to translational base disturbances, due to the fact that a direct mechanical linkage exists between the base and payload. The ASPS, on the other hand, has a very pronounced high-frequency rolloff due to the "soft" AVS translational loops. This attenuation illustrates the concept of isolation. The low-frequency response characteristics of both systems have the same shape; however, the ASPS response is 60 decibels better in

this region than is the AGS response. This remarkable improvement in error peaking can be attributed to three sources: the significant increase in pointing-loop bandwidth achieved with the ASPS, the attenuated level of disturbance seen by the magnetic pointing loop at the peak frequency, and the use of feed-forward commands in the ASPS configuration to compensate disturbance induced payload torques. Of course, the relatively low bandwidth of the translation loops which attenuate the disturbance levels also make it possible to increase the pointing-loop bandwidth. Thus, the two effects (attenuated disturbance and larger bandwidths) have to be viewed together. The component of pointing-error improvement due to these effects can be regarded as a direct benefit of adding a magnetic pointing interface to the flexible gimbal configuration.

REFERENCES

1. Anderson, W.W.; and Joshi, S.M.: The Annular Suspension and Pointing (ASP) System for Space Experiments and Predicted Pointing Accuracies. NASA TR-448, December 1975.

2. Flexibility Effects Analysis. Control Dynamics Corporation, Huntsville, Alabama. Sperry Publication No. 71-1747-48-00, March 1982.

3. AGS Control System Design and Pointing Performance Report. Sperry Publication No. 71-1741-00-01, December 1982.

4. Kochenburger, Ralph J.: Computer Simulation of Dynamic Systems. Prentice-Hall, Inc, 1972.

5. Hamilton, Brian J.: Stability of Magnetically Suspended Optics in a Vibration Environment. Sperry Publication No. 69-1554-02-00, June 1981.

1. Report No.	2. Government Accession No.	3. Recipient's Catalog No.
172481		

4. Title and Subtitle	5. Report Date
Impact of Magnetic Isolation on Pointing System Performance in the Presence of Structural Flexibility	February 1985
	6. Performing Organization Code: 07187

7. Author(s)	8. Performing Organization Report No.
J. Sellers	
	10. Work Unit No.

9. Performing Organization Name and Address	11. Contract or Grant No.
Sperry Corporation Space Systems Division Phoenix, Arizona 85036	NAS1-16909
	13. Type of Report and Period Covered

12. Sponsoring Agency Name and Address	14. Sponsoring Agency Code
National Aeronautics and Space Administration Langley Research Center, Virginia	

15. Supplementary Notes

16. Abstract

A study has been conducted to compare the inertial pointing stability of a gimbal pointing system, (AGS), with that of a magnetic pointing/gimbal followup system, (ASPS), under certain conditions of system structural flexibility and disturbance inputs from the gimbal support structure. Separate 3 degree-of-freedom (3DOF) linear models based on NASTRAN modal flexibility data for the gimbal and support structures were generated for the AGS and ASPS configurations. Using the models inertial pointing control loops providing 6dB of gain margin and 45° of phase margin were defined for each configuration. The pointing loop bandwidth obtained for the ASPS is more than twice the level achieved for the AGS configuration. The AGS limit can be directly attributed to the gimbal and support structure flexibility.

As a result of the higher ASPS pointing loop bandwidth and the disturbance rejection provided by the magnetic isolation ASPS pointing performance is significantly better than that of the AGS system. Specifically, the low frequency (non modal) peak of the ASPS transfer function from base disturbance to payload angular motion is almost 60dB lower than AGS low frequency peak.

17. Key Words (Suggested by Author(s))	18. Distribution Statement
AGS, Gimbal, Magnetic Pointing, ASPS, Flexibility, Modal Data	

19. Security Classif. (of this report)	20. Security Classif. (of this page)	21. No. of Pages	22. Price

N-305

For sale by the National Technical Information Service, Springfield, Virginia 22161

DISTRIBUTION LIST

NASA Contractor Report 172481

NAS1-16909-T2

Address	Number of Copies
NASA Langley Research Center Hampton, VA 23665	
Attn: 152/W. W. Anderson	1
161/A. Fontana	1
433/J. C. Gowdey	1
494/N. J. Groom	1
107/E. B. Pritchard	1
161/L. W. Taylor, Jr.	1
364/W. R. Hook	1
161/C. R. Keckler	20
151A/Research Information Office	2
NASA Goddard Space Flight Center Greenbelt, MD 20771	
Attn: 716.2/P. A. Studer	1
711.2/G. E. Rodriguez	1
712.0/K. Dolan	1
420.0/R. Volpe	1
Library	1
NASA Marshall Space Flight Center Marshall Space Flight Center, AL 38512	
Attn: JA51/Rein Ise	1
JA53/John Owens	1
JA52/Dwight Johnston	1
EB22/Paul Golley	1
ED15/Harry Buchanan	1
EE91/Harvey Shelton	1
EL54/Douglas Nixon	1
EL54/Robert Smith	1
AS24L/Library	1
Jet Propulsion Laboratory 4800 Oak Grove Drive Pasadena, CA 91103	
Attn: 198-112A/David Lehman	1
264-235/William Purdy	1
264-235/Ken Russ	1
T-1201/Edward Mettler	1
111-113/Library	1

DISTRIBUTION LIST (cont)

Address	Number of Copies
National Aeronautics and Space Administration Washington, DC 20546	
Attn: RC/Lee Holcomb	1
RC/Duncan McIver	1
RS/Leonard A. Harris	1
S/Richard F. Carlisle	1
S/John D. Hodge	1
United States Air Force Space Division P.O. Box 92960 Worldway Postal Center Los Angeles, CA 90009	
Attn: SD/YNSS/Major J. Bailey	1
SD/YNSS/Lt W. Possell	1
NASA Ames Research Center Moffett Field, CA 94035	
Attn: Library, Mail Stop 202-3	1
NASA Dryden Flight Research Facility P.O. Box 273 Edwards, CA 93523	
Attn: Library	1
NASA Lyndon B. Johnson Space Center 2101 Webster Seabrook Road Houston, TX 77058	
Attn: JM2/Technical Library	1
NASA Lewis Research Center 21000 Brookpark Road Cleveland, OH 44135	
Attn: 60-3/Library	1
NASA John F. Kennedy Space Center Kennedy Space Center, FL 32899	
Attn: NWSI-D/Library	1
NASA Scientific and Technical Information Facility 6571 Elkridge Landing Road Linthicum Heights, MD 21090	15 plus original